J. Fluid Mech. (2007), *vol.* 589, *pp.* 215–252.
doi:10.1017/S0022112007007628 Printed in the United Kingdom

Transient and steady state of a rising bubble in a viscoelastic fluid

SHRIRAM B. PILLAPAKKAM[1], PUSHPENDRA SINGH[1], DENIS BLACKMORE[2] AND NADINE AUBRY[3]

[1]Department of Mechanical Engineering, New Jersey Institute of Technology, Newark, NJ 07102, USA

[2]Department of Mathematical Sciences, New Jersey Institute of Technology, Newark, NJ 07102, USA

[3]Department of Mechanical Engineering, Carnegie Mellon University, Pittsburgh, PA 15213, USA

(Received 18 January 2006 and in revised form 22 May 2007)

A finite element code based on the level-set method is used to perform direct numerical simulations (DNS) of the transient and steady-state motion of bubbles rising in a viscoelastic liquid modelled by the Oldroyd-B constitutive equation. The role of the governing dimensionless parameters, the capillary number (Ca), the Deborah number (De) and the polymer concentration parameter c, in both the rising speed and the deformation of the bubbles is studied. Simulations show that there exists a critical bubble volume at which there is a sharp increase in the terminal velocity with increasing bubble volume, similar to the behaviour observed in experiments, and that the shape of both the bubble and its wake structure changes fundamentally at that critical volume value. The bubbles with volumes smaller than the critical volume are prolate shaped while those with volumes larger than the critical volume have cusp-like trailing ends. In the latter situation, we show that there is a net force in the upward direction because the surface tension no longer integrates to zero. In addition, the structure of the wake of a bubble with a volume smaller than the critical volume is similar to that of a bubble rising in a Newtonian fluid, whereas the wake structure of a bubble with a volume larger than the critical value is strikingly different. Specifically, in addition to the vortex ring located at the equator of the bubble similar to the one present for a Newtonian fluid, a vortex ring is also present in the wake of a larger bubble, with a circulation of opposite sign, thus corresponding to the formation of a negative wake. This not only coincides with the appearance of a cusp-like trailing end of the rising bubble but also propels the bubble, the direction of the fluid velocity behind the bubble being in the opposite direction to that of the bubble. These DNS results are in agreement with experiments.

1. Introduction

The motion of a bubble rising in a viscoelastic fluid is one of the classical research problems in the field of non-Newtonian fluid mechanics. From a fundamental viewpoint, this problem is interesting due to (i) the presence of a negative wake at the trailing edge, (ii) the loss of fore–aft symmetry due to the formation of a cusp-shaped trailing end and (iii) an apparent discontinuity in the steady-state velocity as a function of the bubble volume.

It is known that for certain parameter values the wake behind a bubble rising in a viscoelastic fluid can be negative. The wake is called 'negative' because the velocity in the wake (see figure 1) very close to the trailing end is in the direction of the motion

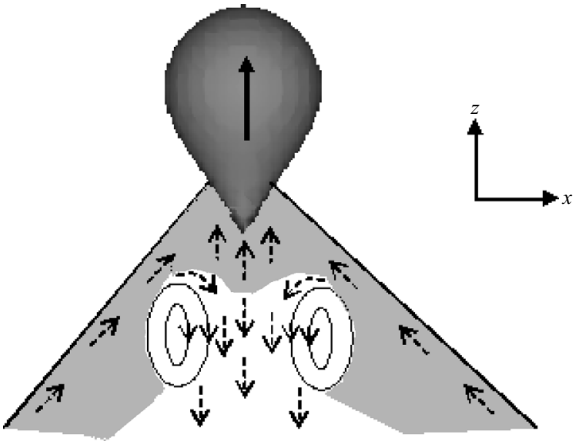

FIGURE 1. Sketch of the velocity vectors in the wake of a bubble rising in a viscoelastic fluid. In the shaded region directly below the trailing end and close to the vertical axis of the rising bubble, the velocity vectors are in the direction of the motion of the bubble. Slightly further away from the trailing end, the velocity is in the opposite direction. Hence, the wake is said to be negative.

of the bubble, but slightly further away from the trailing end the velocity reverses direction. For a bubble rising in a Newtonian liquid, the wake is normal, in that the velocity in the wake is in the same direction as the motion of the bubble, causing an additional drag force opposed to the motion of the bubble.

Hassagar (1979) was the first to observe this behaviour and coined the term *negative wake*. Negative wakes are also observed for spheres falling in viscoelastic liquids (see Arigo & McKinley 2001 and references therein).

Funfschilling & Li (2001) used particle image velocimetry (PIV) and Bisgaard (1983) laser Doppler anemometry (LDA) to investigate the detailed flow field behind rising bubbles in viscoelastic liquids. From their PIV images, Funfschilling & Li (2001) noted the presence of three distinct zones around a rising bubble: a central downward flow zone behind the bubble or negative wake, a conical upward flow surrounding the negative wake zone and an upward flow zone in front of the bubble. Bisgaard (1983) analysed the flow around a rising bubble and a falling sphere, and observed that the negative wake is much closer to the trailing end of a bubble than it is to the trailing end of a solid sphere.

The second interesting feature of a bubble rising in a viscoelastic fluid is that there is a critical bubble volume above which the bubble develops a cusp-shaped trailing end. Philippoff (1937) was the first to notice this phenomenon (also see Rodrigue, Chhabra & Fong 1998, and references listed therein). Liu, Liao & Joseph (1995) performed experiments for bubbles rising in viscoelastic fluids, inside columns of different cross-sections and found that the bubble trailing end is not axisymmetric. Specifically, when the bubble is viewed from the side a cusp can be observed in the wide window and a broad trailing edge appears in the narrow window. A bubble with volume smaller than the critical value assumes either a prolate or an oblate shape depending on the Reynolds number.

Astarita & Apuzzo (1965) noted that, in addition to the aforementioned shape change, "the steady state velocity-volume curve in highly elastic liquids shows a striking peculiarity: a critical volume exists corresponding to an abrupt increase in the velocity". They studied terminal velocities of bubbles rising in four different liquids:

aqueous solutions of carbopol which is a purely viscous and highly pseudoplastic liquid, aqueous solutions of carboxy methyl cellulose-CMC which is slightly elastic, an aqueous solution of ET497 which is highly elastic, and an aqueous solution of J100, a fluid rheologically similar to ET497. The gas bubbles rising in viscous carbopol and slightly elastic CMC solutions deform from a spherical to an oblate ellipsoidal shape and then to a spherical cap with increasing volume, in a manner qualitatively similar to the deformation of bubbles rising in Newtonian liquids. Bubbles rising in highly elastic liquids (i.e. those containing ET497 or J100) deform from spherical to prolate shapes with marked cusp-shaped trailing edges for increasing volume. Moreover, at a critical volume v_c, there is an abrupt increase in the rise velocity, which varies between 2.2 to 5.86 times the velocity before the onset of the increase, depending on the percentage of polymer added to the solution. They further noted that "The shape of the bubble also undergoes a transition at v_c, although not very marked at critical volume when $v < v_c$, although the rear pole is cuspidal, the whole bubble surface appears to be convex. In contrast to this, when $v > v_c$, the protruding tip at the rear pole is more marked and the bubble surface appears to be concave along an horizontal circle slightly above the protruding tip". They explained that this abrupt increase in the velocity is due to the transition from the Stokes regime† to the Hadamard regime.† They suggested that the discontinuity in the rise velocity is due to the presence of surface-active impurities that immobilize small bubbles. Since a similar transition in Newtonian liquid is not accompanied by an abrupt increase in rise velocity, they concluded that viscoelasticity is responsible for this transition. It was shown that for a Newtonian fluid the terminal velocities in the two regimes differ by a factor of 1.5.

Following the work of Astarita & Apuzzo (1965), several researchers investigated this phenomenon experimentally: Barnett, Humphrey & Litt (1966), Calderbank *et al.* (1970) and Leal, Skoog & Acrivos (1971) compared the terminal velocities for rising bubbles and falling glass spheres in a Separan-AP30 solution ranging in concentration from 0.04 % to 1 % by weight. The density of the sphere was chosen to match the terminal rise velocity of an air bubble. Since they did not observe any jump in the velocity of the sphere, they concluded that the observed velocity discontinuity for a bubble at the critical volume is due to a change in the boundary condition at the interface from no-slip to shear free. They also analysed the relative importance of the contributions of shear-dependent viscosity and viscoelasticity to the discontinuity and suggested that a "relatively modest elastic contribution to force balance at the interface would be sufficient to explain the experimentally observed discontinuity".

Liu *et al.* (1995) proposed an alternative explanation for the discontinuity in the rise velocity at the critical volume for bubbles rising in a 1.5% aqueous polyox solution inside channels with rectangular, square and circular cross-sections. They argued that the jump in the rise velocity is due to a reduction in the drag, which occurs due to a change in the bubble shape. They noticed that the bubbles below the critical volume were prolate and those above the critical volume were pointed with a cusp-like trailing end. A few years later, Belmonte (2000) observed experimentally that the discontinuity in the velocity–volume plot occurred at the same volume at which the cusp appeared for a bubble rising in a standard weakly elastic power-law fluid.

† According to Astarita & Apuzzo (1965), "A gas bubble moves in the Stokes regime when the liquid is in creeping flow, the bubble is spherical, and the interface is rigid. A gas bubble moves in the Hadamard regime when the liquid is in creeping flow, the bubble is spherical, and the interface is free".

Name	Magnitude of jump	Conclusions
Astarita & Apuzzo (1965)	~6	Discontinuity is due to transition from Stokes to Hadamard regime
Liu *et al.* (1995)	~10	Discontinuity is due to a sharp reduction in the drag due to cusping
Belmonte (2000)	~4	Discontinuity coincides with cusp formation
Herrera-Velarde *et al.* (2003)	~2.4	Only for bubbles with volumes greater than the critical volume was the negative wake observed; discontinuity is due to the presence of a negative wake

TABLE 1. Summary of the magnitude of the jump in the terminal velocity of a rising bubble and the reasons given for the jump.

Wagner, Giraud & Scott (2002) developed a two-dimensional lattice-Boltzmann scheme for a convected Jeffreys constitutive model for two-phase flows and used this method to simulate bubbles rising in viscoelastic fluids. Although they were able to reproduce the cusp-shaped trailing ends, they did not observe a jump in the magnitude of the velocity as observed in the experiments conducted by Liu *et al.* (1995). Based on their results, they concluded that "the discontinuity observed in experiments was due to the presence of impurities or surfactant molecules that were absent in their numerical simulation".

Herrera-Velarde *et al.* (2003) analysed the flow around bubbles using particle image velocimetry (PIV) for bubbles with a volume close to the critical volume at which the discontinuous change in rise velocity occurs. They reported that when the bubble volume is smaller than the critical volume, the flow resembles that of a bubble rising in a Newtonian fluid, i.e. the velocity in the wake of the rising bubble is positive. For bubbles with volumes greater than the critical volume, they observed a markedly modified velocity distribution and a negative wake.

The presence of surface-active agents affects the surface tension and, consequently, the rise velocity and the jump in velocity at a certain critical volume. Rodrigue, Chhabra & Chan Man Fong (1996) experimentally investigated the effects of surfactants on the velocity of a bubble rising in a viscoelastic fluid. They analysed the effects of various concentrations of sodium dodecyl sulphate (SDS), an ionic surfactant, on four different viscoelastic fluids: 1 mass% CMC, 1 mass% gellan gum (GEL) in distilled water, 3 mass% polyethylene oxide, and ployacrylamide AP-237 (concentration varying between 0.075 and 0.25). They concluded that surface-active agents and elastic forces must be simultaneously present in order to modify the surface and generate a sudden jump in the bubble rise velocity.

A summary of published results concerning the discontinuous jump at the critical volume, which is defined to be the ratio of the velocities after and before the jump, is presented in table 1.

In the past few years, considerable advances have been made in understanding the transient motion and the presence of a negative wake behind spheres falling in viscoelastic liquids. Detailed numerical simulations as well as experimental results and elegant explanations have been reported for the falling sphere problem. A review of the articles published on the settling sphere problem can be found in McKinley (2001). The transient motion of a bubble rising in a viscoelastic fluid, however, has not been investigated as intensively as that of a falling sphere.

Handzy & Belmonte (2003) analysed the transient oscillatory motion of air bubbles rising in a micellar system consisting of an aqueous solution of cetylpyridinium chloride (CPCl) and sodium salicylate (NaSal). For a fixed ratio of [NaSal]/[CPCl] and concentrations from 4 to 40 mM, they analysed the transient behaviour of bubbles with volumes ranging from 14 mm^3 to 110 mm^3 in cylindrical tanks. They observed that when the concentration of [NaSal]/[CPCl] is between 5 mM and 15 mM, bubbles form cusp-shaped tails which lengthen as the bubbles rise, during which the velocity of the leading end remains constant. However, the tail suddenly retracts, and the bubble jumps upward and then decelerates to a constant velocity. These oscillations in the rise velocity persist for a rise distance of over 1 m. For higher concentrations between 25 mM and 40 mM, the shape of the entire bubble changes, in contrast to the lower concentrations where only the tail shape changes. Additionally, for intermediate concentrations, no oscillations were observed. They noted that since falling spheres also oscillate (Jayaraman & Belmonte 2003 and Chen & Rothstein 2004) in wormlike micellar fluids, it was unlikely that the surface tension played a role in bubble oscillations, and that "the common aspect to all these oscillations is the non permanence of the macromolecular structures which are responsible for the fluid stress and therefore the drag".

The objective of this paper is to use the DNS approach to study the problem of a Newtonian bubble rising in an Oldroyd-B liquid with constant viscosity, and thus our numerical results are applicable only to those physical experiments in which it is appropriate to model the viscoelastic liquid by the Oldroyd-B constitutive equation. This, for example, is the case for the experiments described in Astarita & Apuzzo (1965) and Liu *et al.* (1995) that were conducted using polymeric liquids with flexible macromolecular chains, except that these fluids are shear thinning. We also note that the Oldroyd-B constitutive model has been used in several past numerical studies to investigate the problem of a sphere sedimenting in a viscoelastic liquid, which is similar to the problem of a rising bubble, except that the bubble's motion is against gravity (King & Walters 1972; Arigo & McKinley 1998; Singh & Joseph 2000; Singh *et al.* 2000). These studies have shown that the Oldroyd-B model correctly predicts the qualitative features, as observed in experiments, of the flow around a sedimenting sphere, including the existence of a negative wake for certain parameter values, and thus the use of that model to study the problem of a rising bubble is likely to be appropriate as well.

While the rise of a bubble in a viscoelastic fluid has been analysed via two-dimensional numerical simulations in the past (Wagner *et al.* 2002 and references therein), a three-dimensional analysis is necessary to fully understand this asymmetrical problem. In this paper we use the three-dimensional code described in Pillapakkam & Singh (2001) to study the rise of a Newtonian bubble in an Oldroyd-B fluid and analyse the transient and steady-state velocity as a function of the rheological parameters of the ambient fluid and the bubble volume.

The outline of this paper is as follows. The governing equations and dimensionless parameters are stated in the next section, which is followed by a brief description of the numerical approach. In § 5, the simulation results are presented and the role played by the viscoelastic parameters in the shape of the bubble, the velocity field in the vicinity of the rising bubble, and the magnitude of the jump in bubble rise velocity at the critical value of the bubble volume are investigated. The presence of the negative wake, the position of the vortex ring downstream of the bubble, and the stresses near the trailing end of the bubble are also investigated.

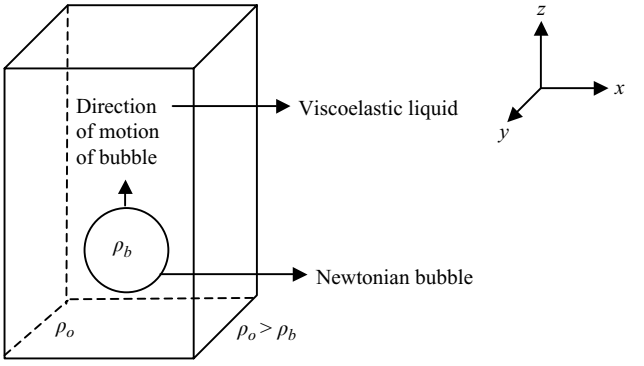

FIGURE 2. Sketch of the three-dimensional computational domain with rectangular cross-section.

2. Problem description and governing equations

Let us consider a fluid bubble, with viscosity η_b and density ρ_b, placed in an ambient fluid with zero shear viscosity η_o and density ρ_o. The ambient fluid will be referred to as the matrix fluid. The bubble is assumed to be immiscible with the matrix fluid. If the densities of the bubble and the matrix fluid are equal, in the absence of an imposed flow the bubble assumes a spherical shape due to the interfacial tension force. If the density of the bubble is smaller than that of the matrix fluid, the bubble will rise due to the buoyancy effect (see figure 2).

In our simulations the motion of the bubble is buoyancy driven and there is no externally imposed velocity field. The bubble, immiscible with the bulk fluid, rises in the bulk fluid due to differences in densities. We analyse the transient and steady-state velocity of a Newtonian bubble rising from a state of rest in a viscoelastic liquid in domains with square and rectangular cross-sections (see figure 2). The viscoelastic fluid is modelled using the Oldroyd-B model.

Let us denote the domain containing the viscoelastic liquid and the bubble by Ω, and the domain boundary by Γ. The governing equations for the two-fluid system are

$$\nabla \cdot \boldsymbol{u} = 0, \tag{1}$$

$$\rho\left[\frac{\partial \boldsymbol{u}}{\partial t} + \boldsymbol{u}\cdot\nabla\boldsymbol{u}\right] = \rho\boldsymbol{g} - \nabla p + \nabla\cdot\left(\eta_s \frac{c}{\lambda_r}\boldsymbol{A}\right) + \nabla\cdot(2\eta_s\boldsymbol{D}) + \gamma\kappa\delta(\phi)\boldsymbol{n}, \tag{2}$$

$$\boldsymbol{u} = 0 \text{ on } \Gamma, \tag{3}$$

so that the domain is a box surrounded by solid walls on which the no-slip boundary condition applies. In order to avoid the effect of the presence of the wall at the top of the domain, the simulations will be stopped when the bubble reaches a constant velocity or when its velocity begins to decrease due to the proximity of the top surface.

The evolution of the configuration tensor $\boldsymbol{A}$ is given by

$$\frac{\partial \boldsymbol{A}}{\partial t} + \boldsymbol{u}\cdot\nabla\boldsymbol{A} = \boldsymbol{A}\cdot\nabla\boldsymbol{u} + \nabla\boldsymbol{u}^{\mathrm{T}}\cdot\boldsymbol{A} - \frac{1}{\lambda_r}(\boldsymbol{A} - \boldsymbol{I}), \tag{4}$$

where $\boldsymbol{u}$ is the velocity, p is the pressure, η_s is the solvent viscosity, ρ is the density, $\boldsymbol{D}$ is the symmetric part of the velocity gradient tensor, c is the polymer concentration parameter, λ_r is the relaxation time of the viscoelastic fluid, $\lambda_r/(1+c)$ is the retardation time, $\boldsymbol{n}$ is the outward normal, γ is the surface tension, κ is the surface curvature,

ϕ is the level-set function defined to be the distance from the interface and δ is the delta function. The zero shear viscosity $\eta_o = \eta_s + \eta_p$, where η_s is the solvent viscosity and $\eta_p = c\eta_s$ is the polymer contribution to viscosity.

The interface position is tracked by using the level-set method (see Sussman, Smereka & Osher 1994 and Pillapakkam & Singh 2001, and references therein). The key idea in this method is to define a scalar variable ϕ, which is equal to the distance from the interface, and convect it with the local velocity, i.e.

$$\frac{\partial \phi}{\partial t} + \boldsymbol{u} \cdot \nabla \phi = 0.$$

3. Dimentionless parameters

The governing equations (1)–(4) are non-dimensionalized by assuming that the characteristic length, time, velocity, pressure and stress scales are a, a/U, U, ρU^2 and ρU^2, respectively. Here U is the volume-averaged velocity of the bubble and a is the radius of the undeformed bubble. Using the same symbols to denote the dimensionless variables, the dimensionless equations can be written in the form

$$\left[\frac{\partial \boldsymbol{u}}{\partial \mathrm{t}} + \boldsymbol{u} \cdot \nabla \boldsymbol{u}\right] = \frac{\boldsymbol{g}}{Fr} - \nabla p + \frac{\eta_s}{\eta_o}\frac{1}{De}\frac{1}{Re}\nabla \cdot (c\boldsymbol{A}) + \frac{\eta_s}{\eta_o}\frac{1}{Re}\nabla \cdot (2\boldsymbol{D}) + \frac{1}{Re}\frac{1}{Ca}\kappa\delta(\phi)\boldsymbol{n}, \quad (5)$$

$$\nabla \cdot \boldsymbol{u} = 0, \quad (6)$$

$$\frac{\partial \boldsymbol{A}}{\partial t} + \boldsymbol{u} \cdot \nabla \boldsymbol{A} = \boldsymbol{A} \cdot \nabla \boldsymbol{u} + \nabla \boldsymbol{u}^{\mathrm{T}} \cdot \boldsymbol{A} - \frac{1}{De}(\boldsymbol{A} - \boldsymbol{I}). \quad (7)$$

The above equations contain the following dimensional parameters: the Deborah number $De = U\lambda_r/a$, which is a dimensionless measure of the relaxation time, the Reynolds number $Re = \rho U a/\eta_o$, which is the ratio of inertial and viscous forces, the capillary number $Ca = U\eta_o/\gamma$, which is the ratio of viscous and surface tension forces, and the Froude number $Fr = U/\sqrt{ga}$, which is the ratio of inertial and gravitational forces. Another useful parameter which gives the relative importance of the inertial and the surface tension forces is the Weber number, $We = Re\,Ca$, or product of the Reynolds and capillary numbers. Two other important parameters are the viscosity ratio η_o/η_b, and the density ratio ρ_o/ρ_b, both of which in this study are assumed to be 10.

4. Numerical scheme

A numerical scheme based on the finite element method, described in Pillapakkam & Singh (2001), is used for solving the time-dependent problem for the motion of a bubble. In this method the governing equations are solved simultaneously everywhere, i.e. both inside and outside the drops/bubbles in the domain. The finite element scheme uses the Marchuk–Yanenko operator-splitting technique to decouple the difficulties associated with the incompressibility constraint, the nonlinear convection term, the interface motion, and the viscoelastic term (Marchuk 1990; Glowinski *et al.* 1999; Singh *et al.* 2000).

Detailed numerical techniques for solving these four sub-problems are described in Pillapakkam & Singh (2001). Here, we will simply note that the operator splitting scheme gives rise to the following four sub-problems: a Stokes-like problem for the velocity and pressure; a nonlinear convection–diffusion problem for the velocity; an advection problem for the configuration tensor; and an advection problem

for the interface. The first problem is solved by means of a conjugate gradient (CG) method (Glowinski *et al.* 1992) and the second is dealt with using a least-square conjugate gradient method (Bristeau, Glowinski & Periaux 1987). The third problem is a hyperbolic partial differential equation for the configuration tensor. The convection term $\boldsymbol{u}\cdot\nabla\boldsymbol{A}$ poses certain numerical difficulties. The two key features of the numerical method used for solving this problem are a scheme that ensures the positive definiteness of the configuration tensor, and a third-order upwinding scheme for discretizing the advection term in the constitutive equation (Singh & Leal 1993). These two features are important for obtaining a split scheme that is stable at relatively large Deborah numbers. The fourth problem consists of the advection of the level-set function ϕ, which is solved using a third-order upwinding scheme (Glowinski & Pironneau 1992). The advected ϕ is then reinitialized to be a distance function, which, as noted in Sussman *et al.* (1994), is essential for ensuring that the scheme accurately conserves mass. The finite element code was validated for several test cases which included the buoyancy-driven motion of a bubble and the deformation of a drop in a simple shear flow (see Pillapakkam & Singh 2001 for more details).

5. Results

A typical computational domain used in this study is shown in figure 2. The velocity on the domain boundary is set to zero, i.e. $u=0$ on all faces of the computational domain. The initial velocities of the bubble and the ambient fluid are assumed to be zero and the configuration tensor is set to $\boldsymbol{A}=\boldsymbol{I}$, which is the relaxed state of the Oldroyd-B fluid. The bubble velocity $u(t)$ is defined to be the volume-averaged velocity of the fluid inside the bubble. Simulations were stopped when the bubble reached a steady state, i.e. the bubble assumed a fixed shape and the rise velocity $u(t)$ became constant. This constant value of the bubble velocity is denoted by U and used as the characteristic velocity for computing the dimensionless parameters.

Simulations are initiated by placing a spherical bubble at a distance of 0.5 cm from the bottom of the domain. The parameters, such as the viscosity, the bubble radius and the polymer concentration parameter, were all varied over a wide range to determine the critical dimensionless parameter values for which the rise velocity of the bubble increases sharply with increasing bubble volume. The results presented in this paper are only for this interesting parameter regime, and presented in terms of the dimensionless parameters, as well as the actual dimensional values used in simulations.

For the results reported in this paper, the density of the ambient liquid is $1\,\mathrm{g\,cm^{-3}}$, the bubble radius was varied between 0.1 and 0.3 cm, and the liquid relaxation time was taken between 0.1 s and 0.2 s. The interfacial tension was held constant at $10\,\mathrm{dyn\,cm^{-1}}$ and the zero-shear viscosity (η_o) was maintained at 10.25 P. The density ratio and viscosity ratio were given the value of 10 for all results presented in this paper. These values were selected to ensure that the computational time needed was not excessive.

Since the viscosity of the ambient fluid affects the rise velocity of the bubble, the zero-shear viscosity was maintained constant and only the relative magnitudes of viscous and viscoelastic contributions to the zero-shear viscosity were varied. This was achieved by varying the polymer concentration factor c in the Oldroyd-B model, which controls the polymer contribution to the zero-shear viscosity (see Singh & Leal 1994). The use of this approach allowed us to focus on the effect of the viscoelastic and viscous components of the ambient viscoelastic fluid on the behaviour of a rising

c	η_o(P)	η_s(P)	η_p(P)
19.5	10.25	0.5	9.75
12.667	10.25	0.75	9.5
9.25	10.25	1	9.25
5.8375	10.25	1.5	8.75
4.125	10.25	2	8.25

TABLE 2. The magnitudes of the solvent (η_s) and polymer (η_p) contributions to the zero-shear viscosity for different values of c, the zero-shear viscosity being $\eta_o = 10.25$ for all cases.

bubble, without having to take into account the additional complications introduced by the change in the bubble velocity due to a change in the ambient fluid viscosity.

The variation in rise velocity with the bubble volume was investigated for five values of the polymer concentration parameter $c = 19.5$, 12.667, 9.25, 5.8375 and 4.125. The relative magnitudes of the polymer (η_p) and solvent (η_s) contributions to the zero-shear viscosity (η_o) for different values of c are shown in table 2. For the range of λ_r, a, and c considered, De varies between $1 \leqslant De \leqslant 6$, $Re \leqslant 0.4$, $Fr < 7.5$ and $We < 4.5$.

5.1. *Convergence of transient and steady results*

We next show that the numerical results obtained for $c = O(10)$ converge as the spatial resolution is increased and the time step used decreased. In figure 3(*a–d*), the rise velocity is plotted as a function of time for different resolutions and time steps. The results are identical for $t < 0.04$ s, but deviate as t increases. The deviation at larger times due to the fact that when the mesh is not sufficiently refined or when the time step is not sufficiently small, there is a decrease in the bubble volume which, in turn, alters the rise velocity of the bubble. However, we find that by increasing the resolution and reducing the time step, the volume can be kept approximately constant. It is critical that the bubble volume does not change since it affects the buoyant lift, the drag, and thus the rise velocity as well. For all results reported in this paper the change in the bubble volume was less than 1%.

5.1.1. *Dependence of the rise velocity on the domain size*

Two computational domains with dimensions $2 \times 2 \times 4$ cm (domain A) and $1.5 \times 1.5 \times 3$ cm (domain B) were used in our simulations. The reason for selecting domains with two different cross-sections is to show that the qualitative dependence of the bubble rise velocity on the bubble volume remains unchanged as the channel cross-sectional area is varied. Note that the experimental results described in Liu *et al.* (1995) were conducted in rectangular columns for which the cross-sectional width was approximately 5 to 10 times the bubble diameter, which is of the same order as the column width used in this study. Although experiments reported in Herrera-Velarde *et al.* (2003) were performed in columns with larger cross-sections, they also showed that the critical volume at which a sharp increase in the rise velocity occurred was approximately independent of the channel width. As we now show, this is also the case for our direct simulations.

Figure 4(*a*), that displays the transient velocity of a bubble of radius 0.125 cm rising in domains A and B, shows that the steady-state velocity in the smaller domain is ~13% smaller and that the velocity at the first overshoot is also smaller. The rise velocity in the smaller domain is thus reduced to a greater extent due to the proximity of the domain sidewalls. The rise velocity in the bigger domain oscillates

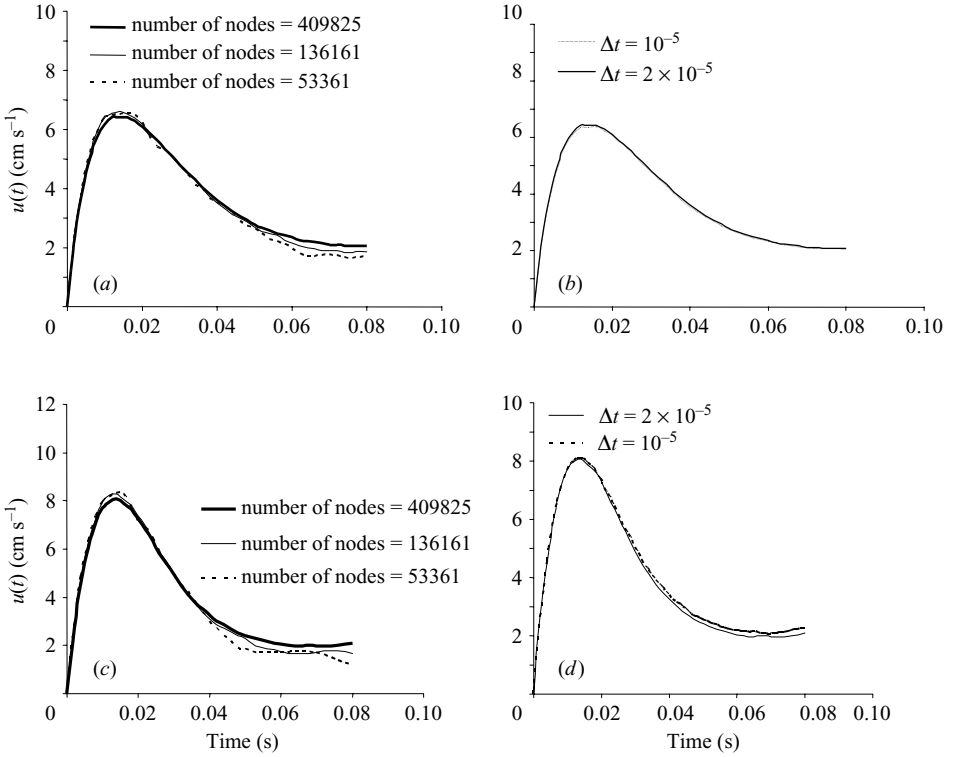

FIGURE 3. (*a*) Convergence with mesh resolution; the parameter values used here are $\eta_o = 10.25$ P, $\lambda_r = 0.1$ s, $c = 4.125$, $a = 0.25$ cm and a time step of 10^{-5}, with the dimensionless parameters $Ca = 5.83$, $Re = 0.14$, $De = 2.27$ and $Fr = 3.63$. (*b*) Convergence with the time step used. The number of nodes is 409825, and the parameters are the same as in (*a*). (*c*) Convergence with mesh resolution; the parameters used here are $\eta_o = 10.25$ P, $\lambda_r = 0.1$ s, $c = 9.25$, $a = 0.25$ cm and a time step of 10^{-5}, with the dimensionless parameters $Ca = 8.71$, $Re = 0.2$, $De = 3.8$, and $Fr = 5.4$. (*d*) Convergence with time step. The number of nodes is equal to 409825, and the parameters are the same as in (*c*).

to a larger extent than in the smaller domain. The fractional decrease in the velocity is qualitatively consistent with the Faxen law (see Happel & Brenner 1981). However, even though the rise velocity is smaller in domain B, the transient behaviour in the two domains is qualitatively similar. Thus, we opted to use the smaller sized domain for the bubbles whose radius is 0.125 cm or smaller for which a higher spatial resolution was necessary around the bubble for obtaining convergent results. We have verified that for all the cases studied in this paper the qualitative transient behaviour of the bubbles was indeed independent of the domain size.

We also investigated the dependence of the rise velocity on the domain size for a range of bubble radii $0.1\,\text{cm} < a < 0.3\,\text{cm}$ and plotted the steady-state velocity as a function of the bubble volume on a log-log plot. The results for domains A and B are shown in figure 4(*b*). From this figure we note that the rise velocity in domain A is larger, which is consistent with the predictions of Faxen's law. The qualitative nature of the terminal velocity versus volume curve, including the critical volume at which the sudden increase in the rise velocity occurs, however, remains unchanged despite the increase in the cross-sectional area.

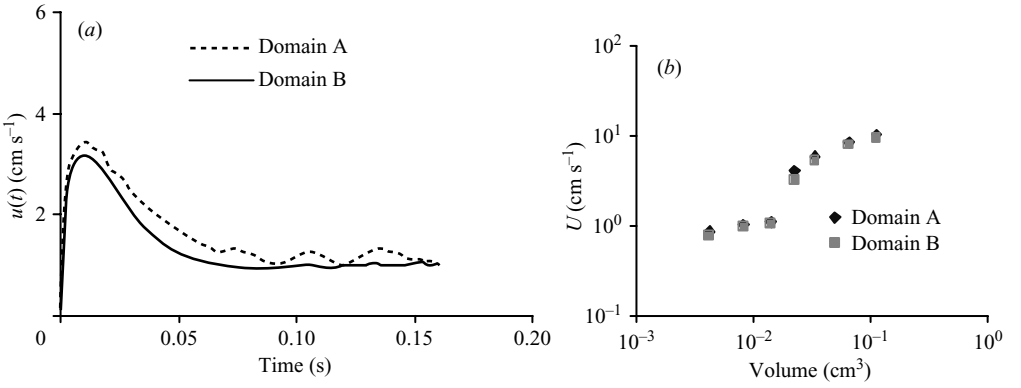

FIGURE 4. (*a*) Transient velocity of bubbles of radius 0.125 cm rising in domain A, with $a/w \sim 0.0625$, and domain B, with $a/w \sim 0.083$, where w is the channel width. The parameters are $\eta_o = 10.25$ P, $c = 4.125$, $\lambda_r = 0.1$ s, $\gamma = 10\,\mathrm{dyn\,cm^{-1}}$, the dimensionless parameters are: $Ca = 1.53$, $Re = 0.01$, $De = 1.2$, and $Fr = 1.35$. The rise velocity in domain A is approximately 13% larger because of the wall effects, which act to reduce the velocity, and are smaller for this domain since its cross-sectional area is larger. (*b*) Terminal velocity versus volume on a log-log plot in domains A and B. The parameters are $\eta_o = 10.25$ P, $c = 9.125$, $\lambda_r = 0.1$ s, $\gamma = 10\,\mathrm{dyn\,cm^{-1}}$.

5.2. *Transient response*

The transient behaviour of a buoyant bubble accelerating from rest in a viscoelastic fluid depends on its volume and the magnitudes of the viscous and viscoelastic stresses, which themselves depend on the fluid properties such as the viscosity and the relaxation time. The bubble is driven by the force of buoyancy, while the viscous and viscoelastic stresses resist its motion. Furthermore, the problem of a rising bubble differs from that of a falling solid sphere, since, in addition to these forces and stresses, the surface tension force acts on the bubble surface, and the shape of the bubble may become non-spherical. If the deforming stresses at the interface are sufficiently smaller than the surface tension force, the bubble shape remains approximately spherical. However, when these deforming stresses are significant the interface deforms and the bubble shape changes depending on the properties of the ambient fluid: it deforms to an oblate shape in inertia-dominated flows and to a prolate shape with or without a cusp-like trailing end in flows in which viscoelasticity is important.

A change in the bubble shape is accompanied by a change in the stress distribution around the bubble which, in turn, affects the net drag acting on the bubble. As a result of these transient interactions between the shape and the stresses, it takes a rising bubble a relatively long period of time to reach a constant rise velocity. Note that this additional interaction between the shape and the stress distribution is obviously not present for a rigid sphere sedimenting in a liquid.

In figure 5 the transient velocities of bubbles of two different sizes are shown as a function of time. All other dimensional parameters are held constant. The figure shows that in both cases the bubble velocity reaches one or two maximal values, decreases and then reaches an asymptotic value. The velocity of the bubble of radius $a = 0.15$ cm decreases to a constant value after an initial overshoot, while that of the larger bubble experiences one or more local maxima before reaching its final value. As discussed below, the transient response of the larger bubble deviates from that of the smaller bubble, as well as from that of a solid sphere, because it deforms due to the extensional nature of the viscoelastic stresses near the trailing end. When

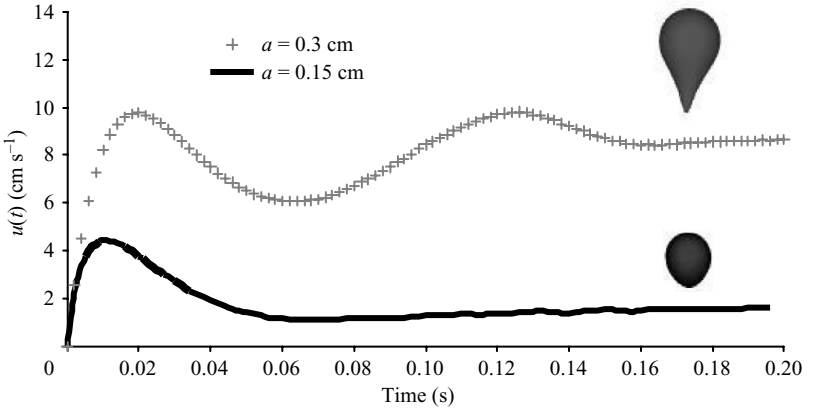

FIGURE 5. The transient velocity of bubbles of radii 0.15 cm and 0.3 cm rising in a viscoelastic fluid with $\eta_o = 10.25$ P, $c = 5.8375$ and $\lambda_r = 0.1$ s, $\gamma = 10\,\mathrm{dyn\,cm^{-1}}$. For $a = 0.15$ cm, after the initial overshoot the bubble decelerates to a constant velocity and attains a steady shape which is prolate. For $a = 0.30$ cm, the bubble develops a cusp-like trailing end and velocity increases before reaching a higher terminal value. The dimensionless parameters for a bubble of radius $a = 0.15$ cm are $Ca = 2.05$, $Re = 0.02$, $De = 1.3$, and $Fr = 1.64$, while those for a bubble of radius $a = 0.3$ cm are $Ca = 9.225$, $Re = 0.26$, $De = 3$, and $Fr = 5.24$.

the interfacial tension dominates, the bubble attains a steady shape that is either approximately spherical or prolate without a pronounced tail, and reaches a constant velocity. However, when the viscous and viscoelastic stresses at the interface overcome the interfacial tension, the bubble develops a cusp-like trailing end, and this change in the bubble shape is accompanied by an increase in velocity, as can be seen from the upper curve in figure 5 (corresponding to a radius $a = 0.3$ cm).

We now describe in detail the transient behaviour of a bubble of radius 0.25 cm for which the response is similar to a bubble of radius of $a = 0.3$ cm developing a cusp-like trailing end. The initial motion of the bubble is dominated by the viscous stresses, as the viscoelastic stresses take some time to build up. The trace of the configuration tensor tr$\boldsymbol{A}$ and velocity distributions at the time marked 1 in figure 6 are displayed in figure 7(a, b). From these distributions shown on the domain midplane we note that the viscoelastic stresses are relatively small, and significant only in a small region around the bubble. The velocity field is similar to that around a bubble rising in a Newtonian liquid with a vortex ring around the bubble. After the viscoelastic stresses build up, the bubble velocity decreases and this causes the first overshoot in the velocity versus time curve of figure 6.

King & Walters (1972) performed an analysis of the unsteady motion of solid spheres in viscoelastic liquids in which they noticed a similar behaviour. Specifically, they observed that the velocity overshoots the steady-state velocity, and that when the viscoelastic contribution becomes significant, the sphere starts to decelerate. The qualitative distribution of tr$\boldsymbol{A}$ in the bubble wake is also similar to that occurring in the case of a solid spherical particle (see Arigo & McKinley 1998 and Singh *et al.* 2000).

Following this rapid initial acceleration, the viscoelastic effects start to become significant, and the bubble begins to decelerate. The distribution of tr$\boldsymbol{A}$ at point 2 marked in figure 6 is shown in figure 8(a). Notice that not only has the maximum value of tr$\boldsymbol{A}$ increased to about 9.0 but also it is now significant in a larger region around the bubble. It is precisely at this point in the rise of the bubble that the structure

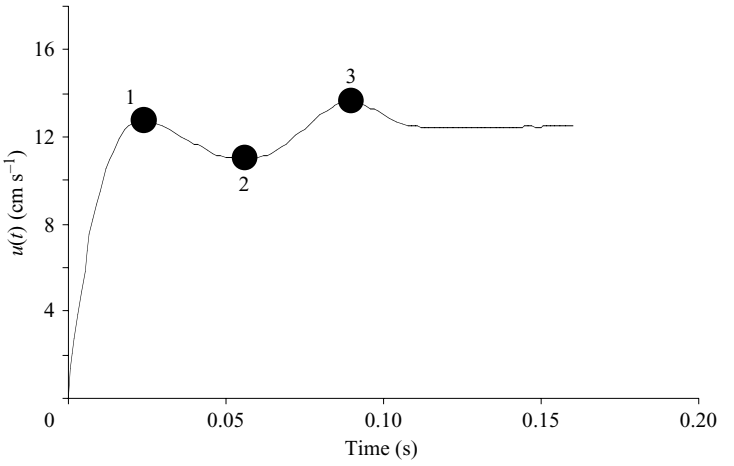

FIGURE 6. Rise velocity $u(t)$ of a bubble of radius 0.3 cm in a viscoelastic fluid with $c = 12.667$, $\lambda_r = 0.2$ s and $\gamma = 10\,\mathrm{dyn\,cm^{-1}}$. The dimensionless parameters are $Ca = 12.37$, $Re = 0.35$, $De = 4.02$, and $Fr = 7.0$.

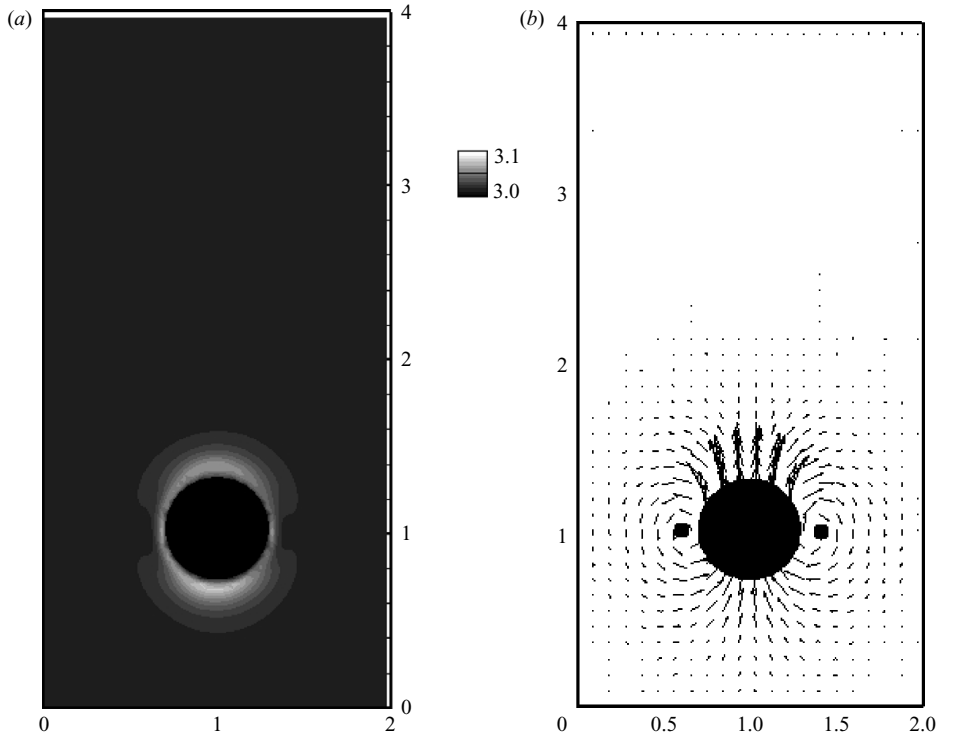

FIGURE 7. (*a*) Isovalues of tr$\boldsymbol{A}$ at time $t \approx 0.02$ s, corresponding to point 1 in figure 6. The parameters are the same as in figure 6. At this time, the maximum value of tr$\boldsymbol{A}$ is 3.1, which occurs at the trailing end of the bubble. Since the maximum value is only slightly greater than 3.0, the viscoelastic stresses are not important at this time. (*b*) Plot of the velocity vectors around the bubble, corresponding to (*a*). Note that at this stage, the velocity in the wake of the bubble is in the direction of the motion of the bubble. The intersection of the centre of the vortex ring and the midplane is indicated by black dots.

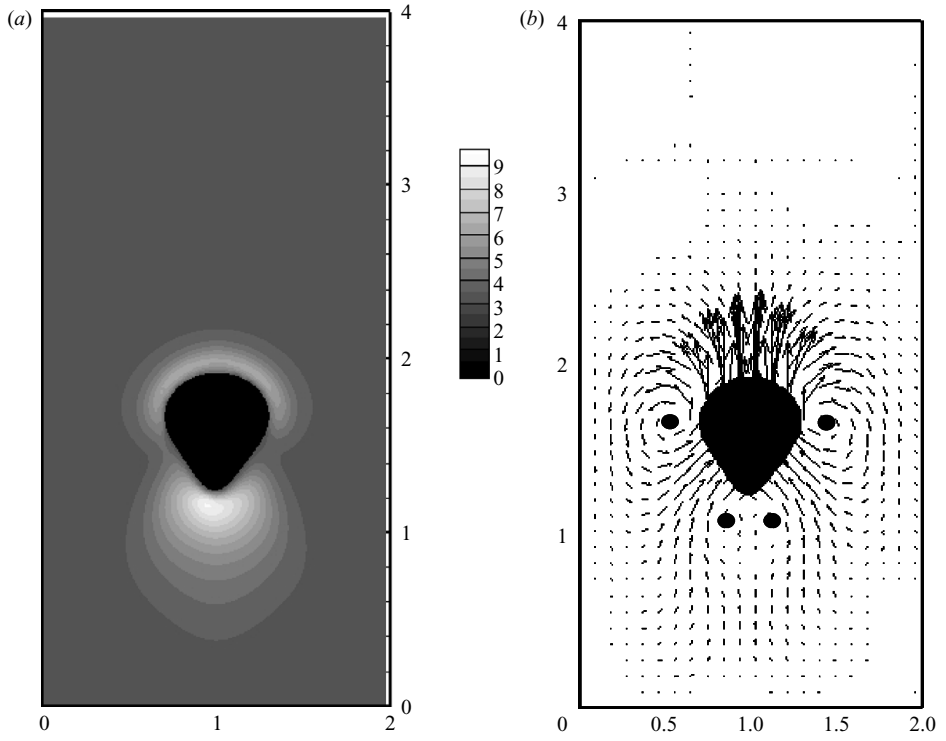

FIGURE 8. (*a*) Isovalues of tr$\boldsymbol{A}$ at time $t = 0.055$ s, corresponding to point 2 in figure 6. The parameters are the same as in figure 6. At this time, the maximum value of tr$\boldsymbol{A}$ is 9.0, which occurs at the trailing end of the bubble. (*b*) Plot of the velocity vectors at the domain midplane, (*a*). Note that at this stage the velocity in the wake of the bubble is in the direction opposite to the direction of the bubble motion. The wake, therefore, is negative. The intersection of the centre of the vortex ring and the midplane is indicated by black dots.

of the wake changes, i.e. the velocity vectors near the trailing end of the bubble are now pointing in the direction opposite to the direction of motion of the bubble (see figure 8*b*). Another interesting feature of the velocity field is the emergence of an additional vortex ring in the wake. The intersection of the centre of this vortex ring with the domain midplane is indicated by black dots and, as the figure shows, it is located at a distance from the bubble of the order of the bubble radius. These changes in the velocity field correspond to the point where the bubble velocity begins to increase again.

As noted above, at the end of the deceleration phase, either the bubble reaches a constant terminal velocity and a steady-state shape which is prolate with a rounded trailing end (see for example the bottom image in figure 5, corresponding to $a = 0.15$ cm) or the bubble undergoes a shape change from prolate to one with a cusp-like tail, while accelerating again to reach a higher terminal velocity. In the former case the nature of the wake is similar to that in the Newtonian case, but in the latter case the wake becomes negative. Thus, there appears to be a connection between the bubble shape and the jump in its rise velocity, which will be discussed in detail below.

For the stage marked 3 in figure 6, the distributions of tr$\boldsymbol{A}$ and velocity field are shown in figure 9(*a*, *b*). Notice that the trailing end of the bubble is now pulled out and the maximum value of tr$\boldsymbol{A}$ takes the large value of 28.0. The region in which

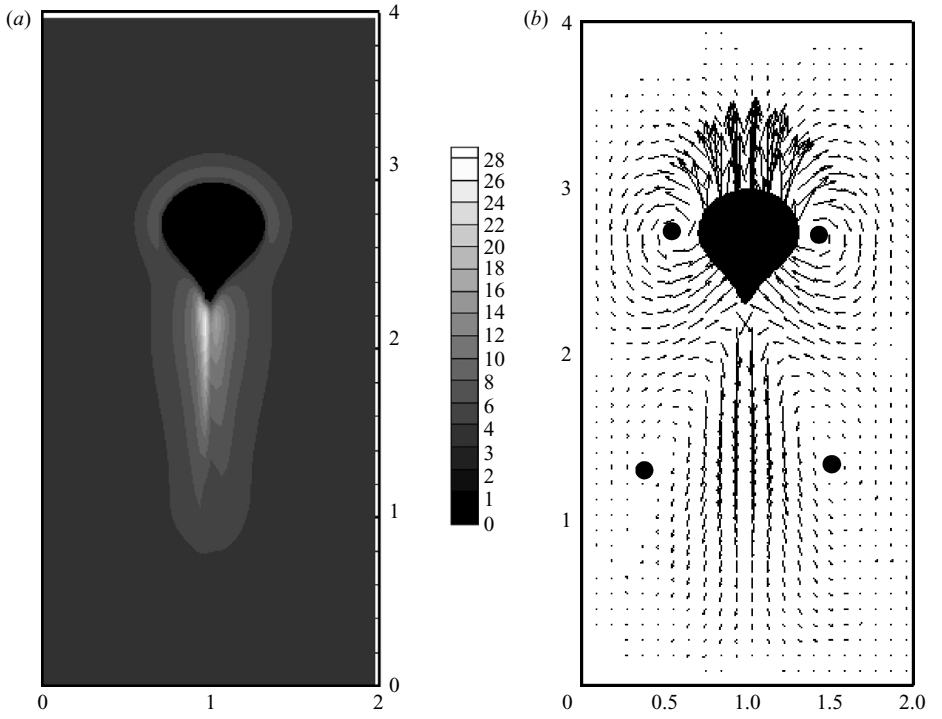

FIGURE 9. (*a*) Isovalues of tr$\boldsymbol{A}$ at time $t = 0.095$ s, corresponding to point 3 in figure 6. The parameters are the same as in figure 6. At this time, the maximum value of tr$\boldsymbol{A}$ is 28.0, which occurs at the trailing end of the bubble. (*b*) Plot of the velocity vectors in the domain midplane corresponding (*a*). It is interesting to note the change in the bubble shape from prolate in figure 8(*b*) to prolate with a cusp-like tail in this figure. Furthermore, the two black dots at the intersection of the vortex ring in the wake and the midplane have now drifted further away below the trailing end of the bubble.

the viscoelastic stresses are significant is much larger than before, and the magnitude of tr$\boldsymbol{A}$ is large in a narrow region emanating from the tail of the bubble. This is consistent with the results obtained in two dimensions by Chilcott & Rallison (1988), and Noh, Kang & Leal (1993) who used a version of the FENE dumbbell model to show that at large Deborah numbers the viscoelastic stresses are large in a thin region at the rear of the bubble and capable of overcoming the surface tension to produce a cusped-like trailing end. Moreover, the velocity vectors show that the wake is negative and that the additional vortex ring has moved away from the bubble (see figures 9 and 10). Also notice that the maximum value of tr$\boldsymbol{A}$ is not along the vertical line emanating from the trailing end and the tr$\boldsymbol{A}$ distribution near the trailing end is not axisymmetric which, as we will discuss later, is a result of the fact that the trailing end itself does not remain axisymmetric.

As the terminal velocity increases with increasing bubble size, the capillary number for the larger sized bubbles is larger making them easier to deform. Similarly, the viscoelastic stresses, which also depend on the rise velocity of the bubble, are also larger for larger bubbles. It can be observed from figure 9(*a*) that the viscoelastic stresses are particularly large near the trailing end of the bubble, and as noted in Pillapakkam & Singh (2001), they are extensional near the trailing end as the

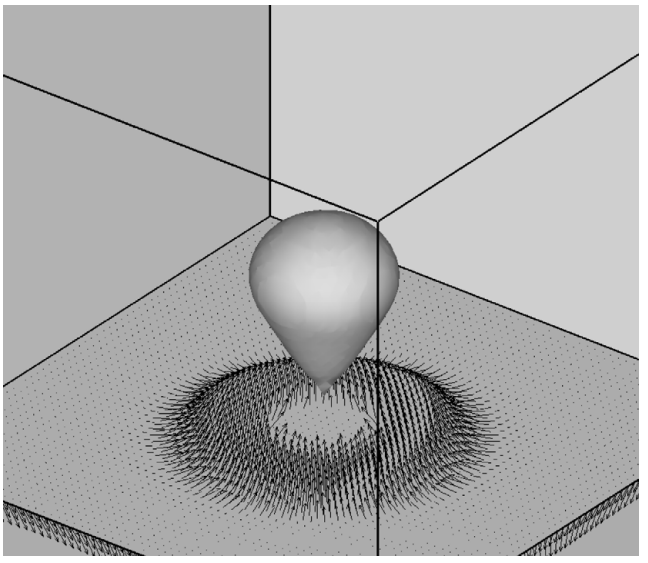

FIGURE 10. The velocity vectors in a plane at a distance of 0.3 cm from the trailing end of the bubble rising in a viscoelastic fluid; the parameters are $\eta_o = 10.25$ P, $\lambda_r = 0.1$ s, $a = 0.35$ cm and $c = 19.5$. In an approximately circular region with dots, directly below the trailing end of the bubble, the velocity vectors point downwards, indicating that the fluid is moving away from the bubble. The wake is therefore negative.

principal direction of the configuration tensor is approximately parallel to the outflow direction (see also Ramaswamy & Leal 1999). Thus, when the viscoelastic stresses are significant the bubble assumes the characteristic prolate shape. We remind the reader that a bubble rising in a Newtonian liquid takes an oblate shape with the trailing end pulled inwards. When the bubble volume is increased further, its trailing end deforms into a cusp-like shape (see figures 5–9).

5.2.1. *Negative wake*

The fluid velocity in the wake of a bubble rising in a viscoelastic fluid, very close to the trailing end, is in the direction of the motion of the bubble. However, at a small distance from the trailing end, the velocity direction reverses. For a bubble rising in a Newtonian liquid, the fluid velocity behind the bubble is in the same direction as the motion of the bubble (see figure 11*a*).

The existence of a cusp-like trailing end, which is sustained by the presence of the surface tension and the extensional viscoelastic stresses, alters the velocity field in the bubble wake. The altered velocity field is such that the wake is negative, while the stresses and the drag for the bubble are modified such that the bubble travels at a much higher velocity than before the trailing edge is pulled out.

The presence of a negative wake can also be seen more clearly in figure 10 where the velocity vectors in a horizontal plane at a distance of 0.3 cm below the trailing end of the bubble are depicted. Arrows indicate vectors pointing out of the plane and dots velocity vectors pointing into the plane. It is seen that velocity vectors point downward in a circular area just below the trailing end of the bubble while they point upward in the surrounding annular region. Since the velocity vectors below the trailing end of the bubble point downward, the wake is negative.

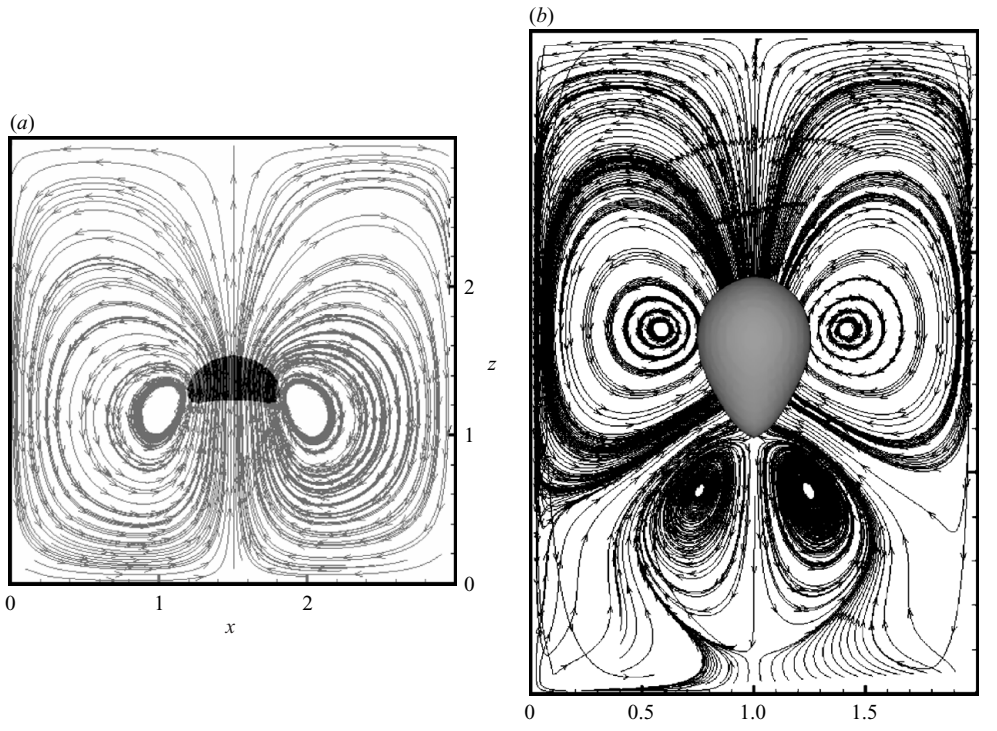

FIGURE 11. (*a*) Stream traces on the domain mid-plane for a bubble rising in a Newtonian fluid with viscosity $\eta = 10.25$ P and a bubble radius $a = 0.3$ cm; $Re = 0.3$, $Ca = 10.25$, and $Fr = 5.8$. Notice that the velocity in the wake is in the upward direction, i.e. in the same direction as the motion of the bubble. (*b*) Stream traces on the domain mid-plane for a bubble rising in a viscoelastic fluid; the parameters are $a = 0.35$, $c = 19.5$, $\eta_o = 10.25$ P and $\lambda_r = 0.1$ s. Notice that in addition to the vortex ring at the equator, there is an additional vortex ring in the wake of the bubble.

As noted above, apart from the vortex ring at the equator of the bubble, which is also present for bubbles rising in Newtonian fluids (see figure 11*a*), there is an additional vortex ring in the wake of a bubble which can be clearly seen in the stream trace plots of figure 11(*b*).

Figure 12 shows that the magnitude of the maximum negative velocity in the wake of the bubble increases as the parameter λ_r or c of the ambient fluid is increased. This is important because, as we will discuss later, when the negative wake is stronger the sharp increase in the bubble rise velocity is larger.

5.2.2. *Transient response as a function of c*

Next, we study the transient response of a rising bubble as a function of c, while keeping the remaining parameters constant. Since η_o is held constant, changing c also requires changing η_p and η_s, such that $\eta_o = \eta_p + \eta_s$ remains constant.

The transient response of a bubble with radius $a = 0.35$ cm rising in a viscoelastic fluid with $\eta_o = 10.25$ P and $\lambda_r = 0.1$ s is displayed in figure 13(*a*) for two different values of c. We note from this figure that the velocity is more oscillatory for the case with a higher value of c, as the viscoelastic stresses are larger when c is larger. This is due to the fact that increasing c increases the viscoelastic component of the total viscosity but reduces the viscous component. Our simulations show that for higher c values, for which the viscous contribution to the viscosity is smaller, the bubble

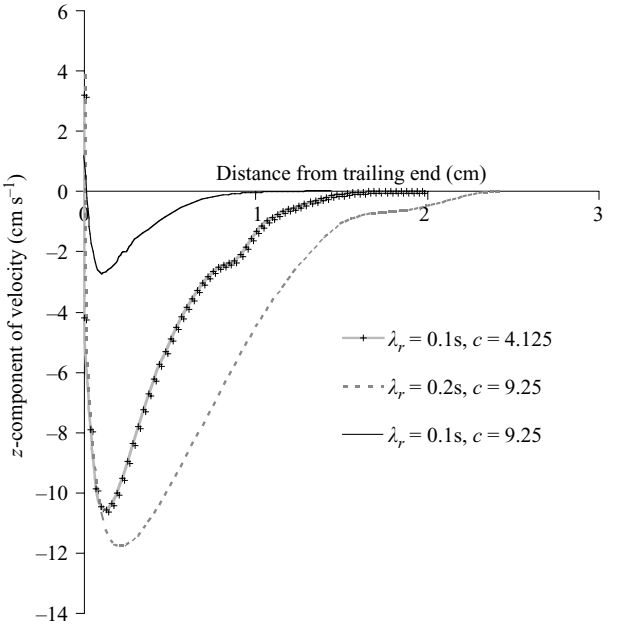

FIGURE 12. The velocity in the wake of a bubble, for a bubble radius $a = 0.25$ cm, rising in a viscoelastic fluid with $\eta_o = 10.25$ P, $c = 4.125$ and 9.25, $\lambda_r = 0.1$ s and $\lambda_r = 0.2$ s.

attains a higher terminal velocity. After the initial overshoot, the bubble velocity starts to decelerate due to the build-up of viscoelastic stresses. For $c = 4.125$, after the deceleration phase, the bubble's rise velocity oscillates only slightly and eventually reaches steady state and the shape remains approximately fixed, while for $c = 9.25$, the velocity continues to oscillate and the shape of the bubble does not reach a steady state. The amplitude of the velocity oscillations decays with time in both cases, but the rate of decay is slower than for the smaller bubble shown in figure 5 for which c and De are relatively smaller. This behaviour indicates that there is an overshoot in viscoelastic stresses, which can occur when c and De are greater than one, and thus the time interval over which the transients persist is larger. This has been observed both in experiments and simulations (see Singh & Leal 1993, 1994, and references therein). Also notice that the response is similar to that of an underdamped mass–spring system which could also be a reason since the Reynolds number is not negligible (we thank a reviewer for suggesting this). It is also interesting to note that due to a relatively higher rise velocity the leading end of the bubble for the larger c case is flattened, which is similar to the deformation of bubbles rising in a Newtonian fluid. Moreover, the maximum value of tr$\boldsymbol{A}$ in the domain is larger for $c = 4.125$, but the region in which it is large is concentrated in a smaller area than for $c = 9.25$ (see figure 13*b*, *c*).

5.2.3. *Transient response as a function of relaxation time*

We next analyse the transient response of a rising bubble as a function of the fluid relaxation time λ_r. The values of c and a are held constant, and $\eta_o = 10.25$. For $\lambda_r = 0.1$ s and 0.2 s the velocity of a bubble with $a = 0.25$ cm is shown in figure 14. The steady-state velocity is higher for the case with $\lambda_r = 0.2$ s, but the magnitude of the overshoot, compared to the approximate steady value, is larger for $\lambda_r = 0.1$ s. Furthermore, in the case where $\lambda_r = 0.2$ s, the peak value of the overshoot occurs at

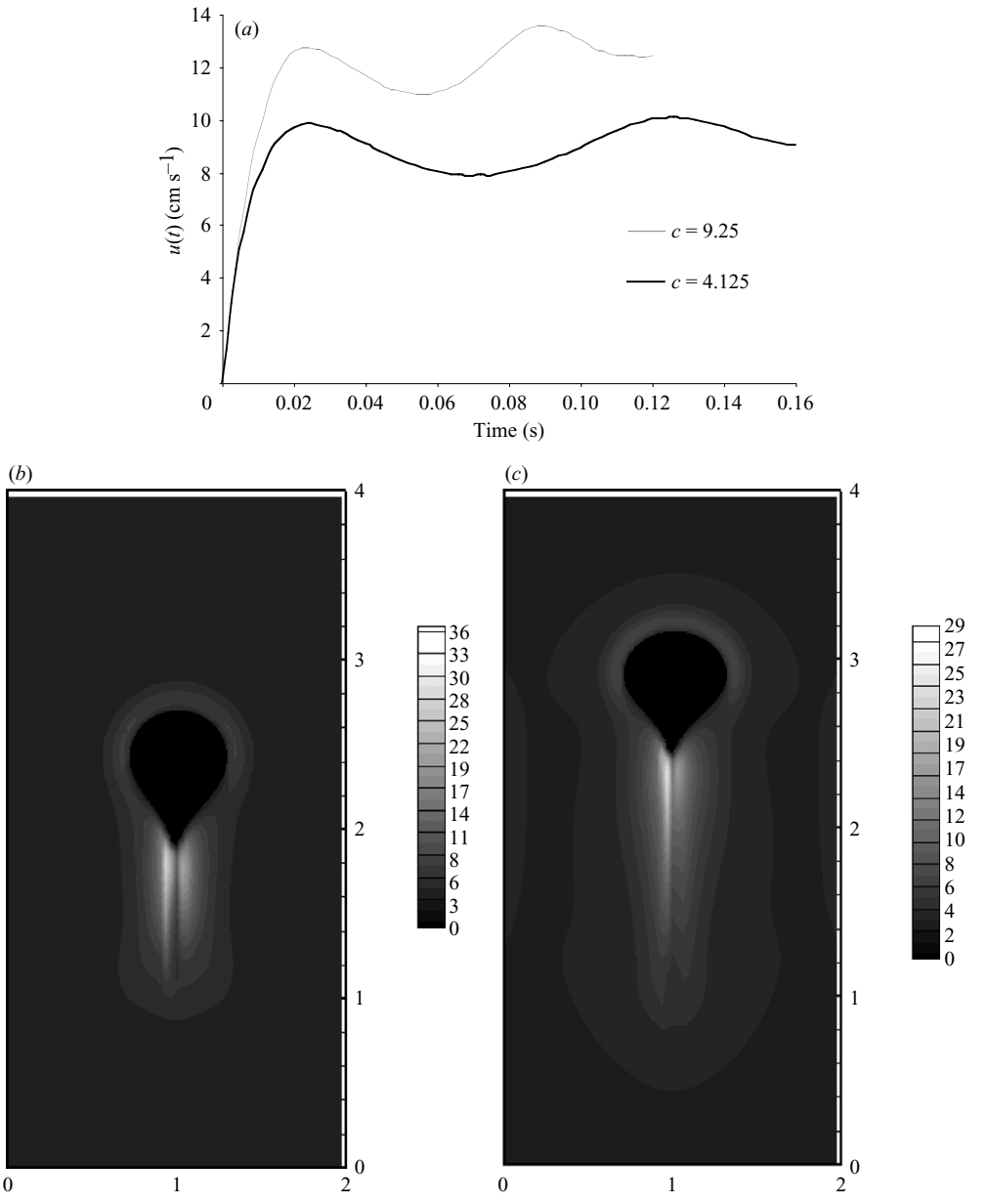

FIGURE 13. (*a*) The bubble rise velocity is shown as a function of time for two different values of c; the parameters are $a = 0.3$ cm, $\eta_o = 10.25$ P and $\lambda_r = 0.2$ s. The dimensionless parameters for the bubble with $c = 4.125$ are $Ca = 9.225$, $Re = 0.26$, $De = 3$, and $Fr = 5.24$, while the bubble with $c = 9.25$ did not reach steady state. (*b*) Isovalues of tr$\boldsymbol{A}$ at steady state for a bubble rising in a viscoelastic fluid for $c = 4.125$. The remaining parameters are as in (*a*). (*c*) Isovalues of tr$\boldsymbol{A}$ at $t = 0.12$ s for a bubble rising in a viscoelastic fluid for $c = 9.25$. The remaining parameters are as in (*a*).

a later time. As discussed in the previous sub-section, the overshoot is due to the viscoelastic stresses taking some time to build up and for the case with larger λ_r, the time interval required for the building up of viscoelastic stresses is larger.

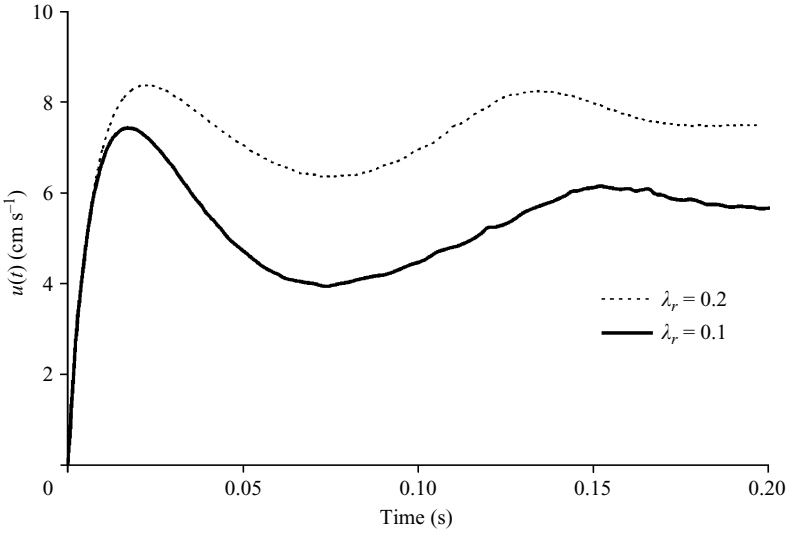

FIGURE 14. The rise velocity $u(t)$ of a bubble for $\eta_o = 10.25$ P, $c = 4.125$, $a = 0.25$ cm and for $\lambda_r = 0.1$ s and 0.2 s. The dimensionless parameters for the bubble rising in a fluid with $\lambda_r = 0.1$ s are $Ca = 5.83$, $Re = 0.14$, $De = 2.27$, and $Fr = 3.63$, while those corresponding to the case where $\lambda_r = 0.2$ s are $Ca = 8.2$, $Re = 0.3$, $De = 5.33$, and $Fr = 4.66$.

As the steady values of the bubble velocity for the above two cases are different, their shapes, as well as the viscoelastic stress distributions around them, are also different. For $\lambda_r = 0.2$ s, the maximum value of tr$\boldsymbol{A}$ is larger and the region in which the viscoelastic stresses are significant is also larger (see figures 13*b* and 15*a*). However, as is clear in these figures, for $\lambda_r = 0.1$ s, the trailing end of the bubble is pulled out further. The local region in the wake of the bubble in which tr$\boldsymbol{A}$ is maximum no longer emanates from the tail, but is maximum at a small distance from the vertical passing through the bubble centre. The value of tr$\boldsymbol{A}$ emanating from the pulled out tail is relatively smaller.

Another interesting aspect of the deformed bubble shape is that the centre of curvature in the domain midplane is no longer inside the bubble, implying that one of the principal radii of curvature is negative. Figure 15(*a*, *b*) shows that the vortex ring below the bubble is farther away from the trailing end of the bubble for $\lambda_r = 0.2$ s. The width of the negative wake region, i.e. the region in which the velocity points away from the bubble, is wider for $\lambda_r = 0.2$ s and the magnitude of the negative velocity is larger.

5.3. *Sharp change in rise velocity as a function of bubble volume*

It has been noted in several past experimental studies that for some viscoelastic liquids the terminal velocity of a bubble increases rather abruptly at a critical value of the bubble volume (Astarita & Apuzzo 1965 and Liu *et al.* 1995 and references therein). Specifically, if the bubble volume is slightly larger than the critical volume, the terminal velocity can be as large as ten times that of a bubble with volume slightly smaller than the critical volume.

Our simulation results are in good qualitative agreement with these experimental observations. We find that when the terminal velocity of a bubble is plotted against the bubble volume, there is a critical volume at which the terminal velocity increases very steeply with increasing volume. This steep increase is analysed below in terms

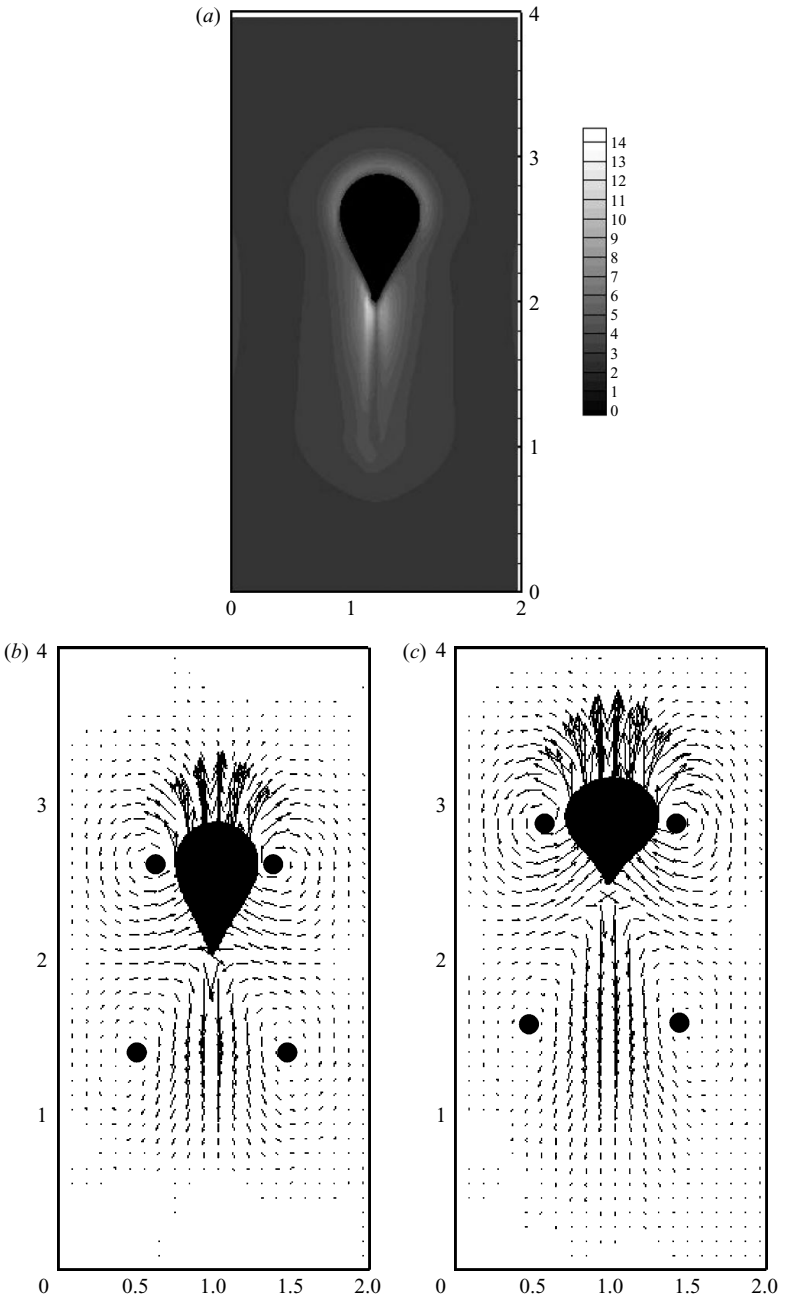

FIGURE 15. (*a*) Isovalues of tr$\boldsymbol{A}$ at steady state for a bubble rising in a viscoelastic fluid for the parameter values $\eta_o = 10.25$ P, $c = 4.125$, $a = 0.25$ cm and $\lambda_r = 0.1$ s. Note that the maximum value of tr$\boldsymbol{A}$, which occurs near the trailing end of the bubble, is approximately 14.0. The dimensionless parameters are the same as in figure 14 for $\lambda_r = 0.1$ s. (*b*) Velocity vectors in the mid-section of the domain illustrating the positions of the vortex rings with respect to the bubble. Note that the vortex ring below the trailing end of the bubble is at a distance of the order of the bubble radius from the bubble. The parameters are $\lambda_r = 0.1$, $c = 4.125$, $\eta_o = 10.25$ P and $a = 0.30$ cm. The dimensionless parameters are the same as in figure 14 for $\lambda_r = 0.1$ s. (*c*) Velocity vectors in the mid-plane at steady state for a bubble rising in a viscoelastic fluid. The parameters are as in figure 14 for $\lambda_r = 0.2$ s. Note that as the relaxation time of the ambient fluid is increased, the distance of the vortex ring from the trailing end of the bubble is greater than in figure (*c*).

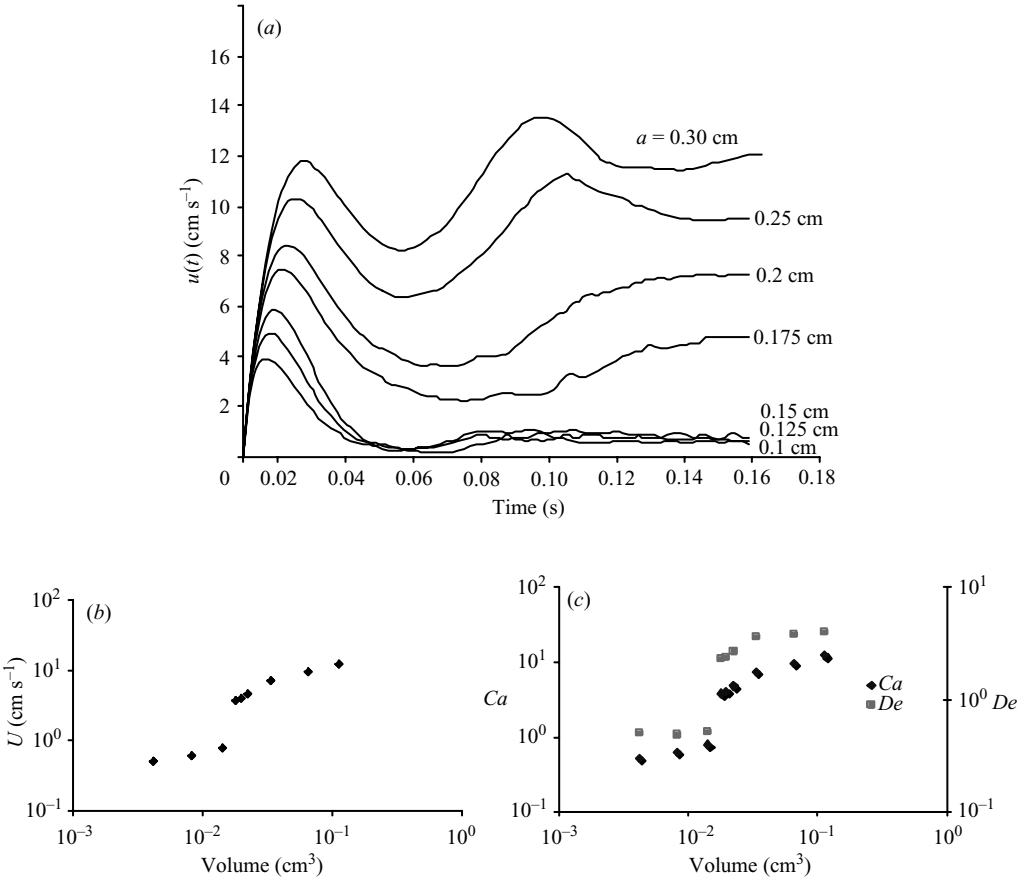

FIGURE 16. (*a*) Transient velocity of bubbles rising in a viscoelastic fluid with $\eta_o = 10.25$ P, $c = 12.667$, $\lambda_r = 0.1$ s, $\gamma = 10$ dyn cm^{-1}. The bubble radius is varied from 0.1 cm to 0.3 cm. (*b*) Terminal velocity versus volume on a log-log plot for the same parameters as (*a*). The terminal velocities of the bubble on the two sides of the sharp increase are 0.78 and 3.75 cm s^{-1}, respectively. The terminal velocity increases by a factor of ~4.8 when the bubble radius is increased by ~8%. (*c*) Capillary number and Deborah number versus volume. Notice that both *Ca* and *De* are $O(1)$ at the critical volume for the same parameters as (*a*).

of the changes that occur (at this critical volume) in the bubble shape and in the velocity distribution around the bubble.

The transient velocities of several bubbles with radii between 0.1 cm and 0.3 cm are shown in figure 16(*a*). The bottom three curves, which correspond to bubbles of radii 0.1 cm, 0.125 cm and 0.15 cm, respectively, attain steady states after the initial overshoot while the velocities for the top four oscillate before reaching steady state. The velocities of the bubbles with $a \geqslant 0.3$ cm continue to oscillate and do not reach a steady value before the bubble reaches the top of the domain.

From figure 16(*b*) in which the steady-state velocity is plotted against the bubble volume on a log-log plot, the terminal velocity of a bubble with $a = 0.1625$ cm is 3.75 cm s^{-1}, which is approximately 4.8 times larger than 0.78 cm s^{-1}, the velocity of a bubble of radius $a = 0.15$ cm. Moreover, while the terminal velocities for the three cases investigated for $a \leqslant 0.15$ cm vary only slightly with the radius, an approximately five-fold increase in the terminal velocity occurs for the relatively small change of

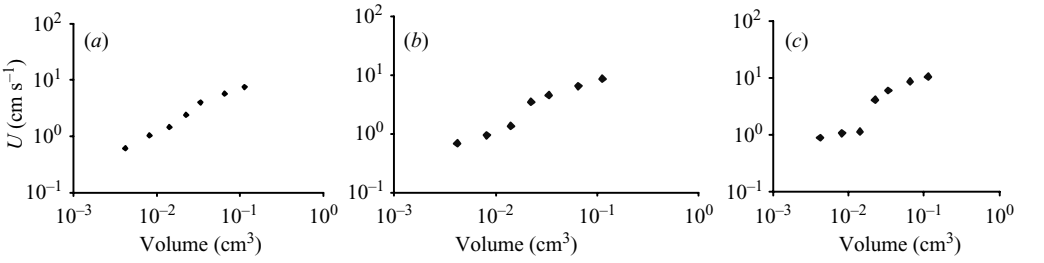

FIGURE 17. Terminal velocity versus volume on a log-log plot for $\eta_o = 10.25$ P, $\lambda_r = 0.1$ s and $\gamma = 10\,\mathrm{dyn\,cm^{-1}}$. (*a*) $c = 4.125$, (*b*) $c = 5.8375$, and (*c*) $c = 9.25$.

c	Magnitude of jump
4.125	1.66
5.8375	2.59
9.125	3.65
12.667	6.02

TABLE 3. Magnitude of the jump for various values of c. The computed jumps are based on the differences in the terminal velocities of the bubbles with radii 0.15 cm and 0.175 cm.

about 8% in the bubble radius when the bubble volume is 0.015 cm^3. Furthermore, figures 16(*c*) shows that the dimensionless parameters Ca and De are $O(1)$ or smaller before the jump, and greater than one after the jump. The Reynolds number, however, remains less than one for all the bubble volumes considered.

Here, it is important to note that since the channel width is only approximately eight times the bubble diameter, the presence of the walls, as discussed earlier, causes a decrease in the bubble rise velocity. The decrease is expected to be larger for the larger bubbles. Therefore, the above five-fold increase in the velocity for about an 8% increase in the bubble radius is clearly not due to the wall effects since the wall effects should make the larger bubble rise slower, and not faster.

Next, we study the dependence of the magnitude of the steep increase in the terminal velocity at the critical bubble volume on the polymer concentration parameter c. It has been noted in Astarita & Apuzzo (1965) and Liu *et al.* (1995) that the magnitude of the jump in the rise velocity at the critical volume increases with increasing polymeric concentration in the solution. Since the zero-shear viscosity of the solutions used in experiments is several times to orders of magnitude larger than that of the solvent itself, it is reasonable to assume that the parameter c for these solutions is of order 10 or larger. The relationship between the polymer concentration parameter c and the actual polymer concentration is, however, simple only when the concentration is very small. At larger polymer concentrations, and even for the so-called moderately concentrated solutions, the relationship is quite complex.

In figures 16(*b*) and 17 the terminal velocity is plotted as a function of the bubble volume for four different values of c. These figures show that the increase in the terminal velocity at the critical volume is steeper for larger values of c. For example, when the bubble radius is increased from 0.15 to 0.175 the terminal velocity increases sharply, and the jump in the bubble velocity increases with increasing c. These results are summarized in table 3. This is consistent with the case of a Newtonian fluid, which corresponds to $c = 0$, and for which the velocity–volume plot does not exhibit

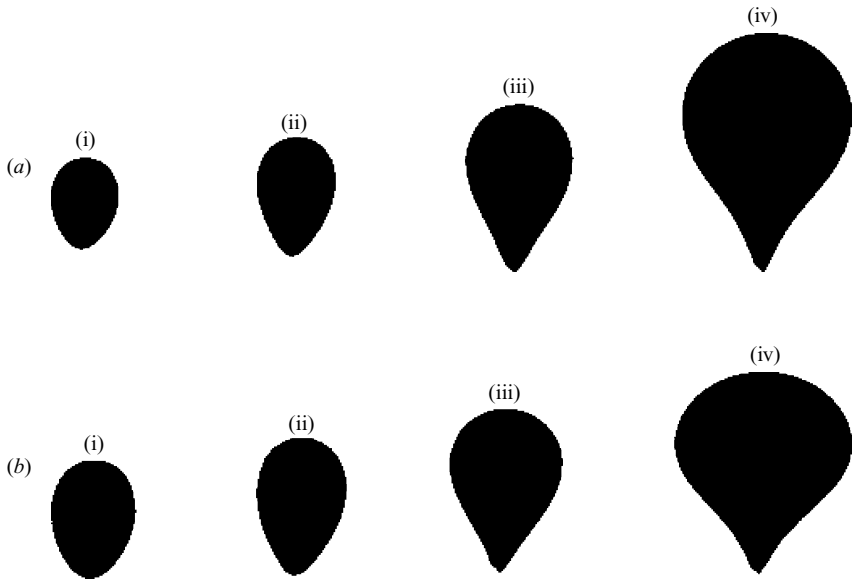

FIGURE 18. (*a*) Steady-state shapes of the bubbles for different volumes rising in a viscoelastic fluid for the parameter values $c = 4.125$, $\lambda_r = 0.2\,\mathrm{s}$, $\eta_o = 10.25$ P. The initial radii are: (i) $a = 0.125\,\mathrm{cm}$ (ii) $a = 0.15\,\mathrm{cm}$ (iii) $a = 0.2\,\mathrm{cm}$ (iv) $a = 0.3\,\mathrm{cm}$. The first two cases correspond to volumes smaller than the critical volume at which the steep increase in bubble velocity is observed. (*b*) As (*a*) but for $c = 9.125$. In comparison with (*a*) the front ends of the bubbles appear flatter, which is a consequence of the terminal velocity increasing with increasing c, and thus the corresponding Reynolds numbers in (*b*) are larger. As a result the front end of the bubble is flattened in a manner similar to the way the front end of bubbles rising in Newtonian fluids flatten.

any region of steep increase. Note that, as stated in § 1, in the case of a Newtonian fluid a jump of 1.5 times in the terminal velocity can arise if the boundary conditions on the bubble surface are changed from no slip to shear free. No jump is reported in the present work since the same boundary conditions are imposed for all bubble volumes.

In our simulations the critical volume, at which a sharp increase in the terminal velocity occurs, does not show a strong dependence on c because the latter is varied so that the zero-shear viscosity remains fixed. The critical volume, however, does depend on the remaining parameters, including the zero-shear viscosity, and the relaxation time (see figure 16).

5.3.1. *Dependence of the bubble shape on the bubble volume*

For the parameter values $c = 4.125$ and $\lambda_r = 0.2\,\mathrm{s}$, the steady-state shapes of the bubble are shown in figure 18(*a*) for four different values of the bubble volume, and in figure 18(*b*) similar results are shown for $c = 9.125$. In both figures the bubble shape for the first two cases, for which the bubble volume is smaller than the critical value, is prolate, and for the last two cases the bubble trailing end is cusp-like. These figures clearly show that the shape of a bubble with volume smaller than the critical volume is fundamentally different from that of a bubble with a volume larger than the critical volume. Also, as the rise velocity of bubbles increases with increasing c, the Reynolds number is larger for the bubbles shown in figure 18(*b*). As a result the fronts of the bubbles shown in figure 18(*b*) are more flattened than those in figure 18(*a*).

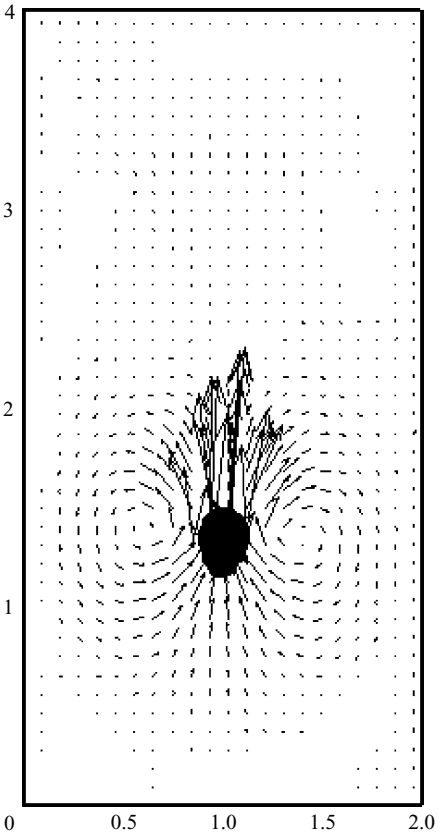

FIGURE 19. Velocity distribution in the domain mid-plane. Notice that the wake is positive since the bubble volume is smaller than the critical volume; the parameters are $a = 0.15$ cm, $\lambda_r = 0.2$ s, $c = 4.125$. All parameters, except for the bubble volume, are the same as in figure 15(c) for which the wake is negative since the bubble volume is larger than the critical volume at which a sharp increase in the rise velocity occurs. This is in agreement with the experimental results of Herrera-Velarde *et al.* (2003).

We have discussed in § 5.2 that our simulation results also indicate that the bubbles for which the velocity oscillates after the initial overshoot experience a change from a prolate shape to one with an extended cusp-like trailing end. In addition, for these bubbles the terminal velocity can be several times larger than for bubbles without extended trailing ends, depending on the value of the parameter c. Thus, the change in the shape of the bubble appears to be one of the reasons for the apparent sharp variation in the terminal velocity at the critical volume. Specifically, bubbles with volumes on either side of the critical volume have markedly different transient behaviours, different deformed shapes, and significantly different terminal velocities, as is evident from comparing the shapes of the bubble on either side of the sharp change in the velocity–volume plot (see figures 16, 17 and 18). We may therefore conclude that the bubble shape plays a critical role in determining the transient as well as the terminal velocity of bubbles rising in viscoelastic fluids.

Another factor that we believe affects the rise velocity of the bubble is the change in the velocity field of the ambient liquid and the presence of the negative wake. The velocity fields of two bubbles with volumes smaller and larger than the critical volume (at which the steep increase in velocity occurs) are shown in figures 19 and 15(c),

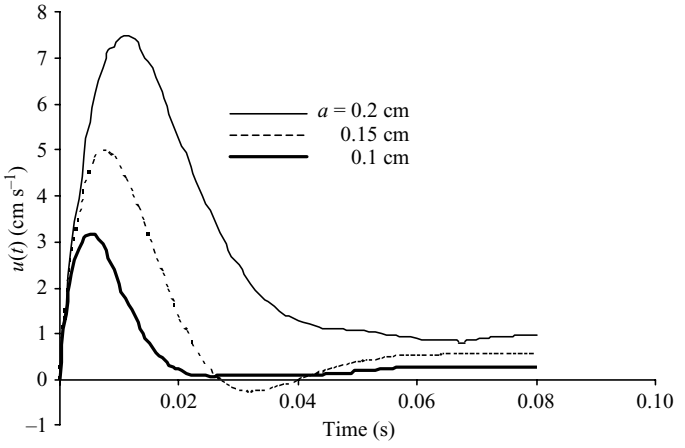

FIGURE 20. $u(t)$ of a bubble rising in a viscoelastic fluid for the parameter values $\eta_o = 10.25$ P, $\lambda_r = 0.1$ s, $c = 19.5$. For the case with $a = 0.15$ cm, the bubble reverses its direction and moves against the direction of buoyancy for a short time interval before the velocity becomes positive again.

respectively. All other parameters for the two cases are identical. The shape of the bubble with radius $a = 0.15$ cm is prolate, while that with radius $a = 0.25$ cm exhibits a pulled-out trailing end. The velocity distributions for the two cases are also quite different. For a bubble of radius $a = 0.15$ cm the direction of motion of the fluid in the wake is the same as that of the bubble, the flow in this case being qualitatively similar to the flow around a Newtonian bubble. For $a = 0.25$ cm, on the other hand, the wake is negative as the direction of fluid motion in the wake is the opposite of that of the bubble and there is an additional vortex ring in the wake. We may therefore conclude that at the critical volume not only the shape of the bubble changes qualitatively, but also the nature of the velocity distribution around it changes fundamentally due to (i) the formation of an additional vortex ring and (ii) the appearance of a negative wake. The appearance of negative wake above the critical volume, as well as the presence of the additional vortex ring, is in agreement with the experimental results reported in Funfschilling & Li (2001) and Herrera-Velarde *et al.* (2003).

5.3.2. *Transient response at higher values of c*

Figure 20 displays the transient velocities of the bubbles of three different radii rising in a viscoelastic fluid with $c = 19.5$. Notice that the overshoots are rather large for all three cases and that for $a = 0.15$ cm the bubble velocity after the overshoot becomes negative for a brief period of time. This implies that the bubble briefly falls before it begins to rise again due to the viscoelastic stresses. This phenomenon has also been observed for solid spheres falling in a viscoelastic upper-convected Maxwell fluid (Zheng & Phan-Thien 1992). They observed that the sphere velocity became negative for a brief period of time when the Wissenberg number was greater than one, which they noted happened because the hydrodynamic drag exceeded the buoyant weight, causing not just the deceleration of the sphere but also a change in the direction of motion. This phenomenon, however, would be difficult to observe in experiments due to the experimental difficulties involved in the generation of a perfectly spherical bubble at the initial time which then, as in simulations, accelerates upwards.

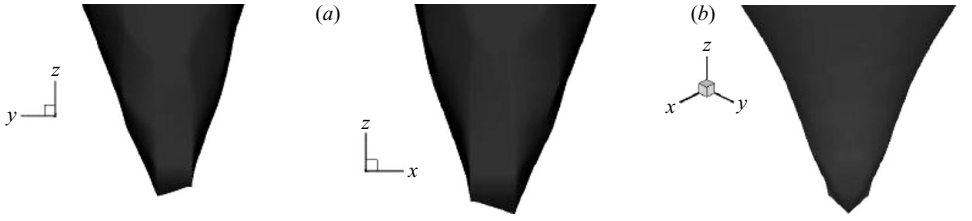

FIGURE 21. (*a*) A magnified view of the trailing end of a bubble rising in a viscoelastic fluid in a domain with a square cross-section. In both x, z- and y, z-views the trailing end appears to be broad. The parameters are $\eta_o = 10.25$ P, $c = 5.8375$, $a = 0.3$, $\lambda_r = 0.1$ s and $\gamma = 10\,\mathrm{dyn\,cm^{-1}}$. (*b*) A pointed cusp-like trailing edge is observed when the bubble is viewed along the cross-sectional diagonal of the computational domain.

5.4. *Bubbles with two-dimensional cusp-like trailing ends*

Liu *et al.* (1995) experimentally studied the rise of air bubbles in viscoelastic liquids inside channels with rectangular and square cross-sections and found that for certain parameter values bubbles develop cusp-shaped trailing ends that appear to have pointed ends in one view and broad ends in the orthogonal view (chisel shaped). Interestingly, they found that in channels with rectangular cross-sections the trailing end appeared to be broad when viewed from the narrow window and pointed when viewed from the broad window. For channels with square cross-sections, they found that the sharp edge of the cusp-shaped trailing end was oriented parallel to one of the cross-section diagonals.

Unlike for the experiments conducted by Liu *et al.* (1995) in which the shape of the trailing edge was different in the two orthogonal views, our simulations lead to bubbles displaying a broad trailing edge in both orthogonal views which, as discussed below, is a consequence of the fact that the spatial resolution used is finite (see figures 21 and 22). This was the case for simulations performed in domains with both square, with dimensions $2 \times 2 \times 4$ cm, and rectangular, with dimensions $2 \times 1.5 \times 4$ cm, cross-sections. However, in domains with square cross-sections, when viewed along the diagonal, the bubble exhibits a pointed trailing end (see figure 21); however, it is not cusp shaped, since the angle formed at the trailing end is not zero.

For channels with rectangular cross-sections, the shape of the trailing end is qualitatively similar to those with square cross-sections, except that a short distance above the tip the width of the tail in the direction parallel to the narrow window is larger than the width parallel to the broad window, which is in qualitative agreement with Liu *et al.* (1995) (see figure 22). The opposite is true at larger distances from the trailing end, which appears to be in agreement with the photographs in Liu *et al.* This latter point, however, is not noted in their paper.

It is clear that our numerical method lacked accuracy in simulating the elongated and narrowed trailing end of the bubble. The reason for this lies in the fact that when the width of the tail, in any of the coordinate directions, becomes smaller than the size of an element it cannot be resolved using the level-set method because it does not allow for two interfaces to be present in one element. Therefore, due to this lack of resolution, even if the governing equations allowed the formation of a cusp at the trailing end, our numerical scheme is not capable of resolving this shape at scales smaller than the size of an element. However, when a mesh with bigger elements was used the trailing-end shape appeared closer to that observed in experiments.

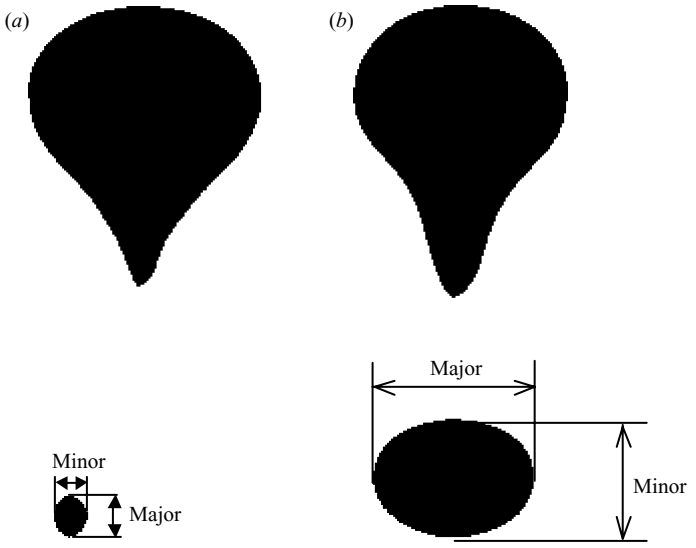

FIGURE 22. Magnified view of the bubble rising in a viscoelastic fluid in a domain with a rectangular cross-section, with dimensions $2 \times 1.5 \times 4$ cm. (*a*) View from broad window (top) and section view of the trailing end at a distance of $0.02a$ above the trailing end tip. In both views, the trailing end appears to be rather broad. The parameters are $\eta_o = 10.25$ P, $c = 5.8375$, $a = 0.3$, $\lambda_r = 0.1$ s and $\gamma = 10\,\mathrm{dyn\,cm^{-1}}$. (*b*) View from narrow window (top) and section view of the trailing end at a distance of a above the trailing end. In both sections the trailing end appears to be broad, but at a distance of a the major axis is parallel to the broad side of the cross-section, and at a distance of $0.02a$ it is parallel to the narrow side.

5.4.1. *Stresses near the trailing end*

As discussed in § 5.3, after the extensional viscoelastic stresses at the trailing end of the bubble reach a critical value, the trailing end of the bubble is pulled out. As this takes place, the local radius of curvature decreases and thus the surface tension force, which locally acts in the upward direction, increases. A new balance is reached when the increased surface tension force at the cusp-like (or cornered in the discretized case) trailing end is sufficient to balance the force due to the viscous and viscoelastic stresses.

The existence of a cusp-like, or cornered, trailing end is thus sustained by the presence of the surface tension force and the extensional viscoelastic stresses that alter the velocity field in the wake of the bubble. The altered velocity field is such that the wake becomes negative and the stresses are such that the bubble attains a much higher velocity than before the trailing end was pulled out.

In the discretized case the bubble surface is represented using planar linear elements, and thus the surface tension force which depends on the radius of curvature at the sharp corner remains finite. The same is true for the viscous and viscoelastic stresses near the trailing end (with a sharp corner), shown as a function of the distance from the trailing end in figure 23. Both the velocity gradient $|\nabla \boldsymbol{u}|$ and the $\mathrm{tr}\boldsymbol{A}$ grow as the distance from the trailing end decreases, indicating that the stresses at the trailing end are singular, but they remain finite for the discretized problem. Furthermore, the negative slopes of the two curves $|\nabla \boldsymbol{u}|$ and $\mathrm{tr}\boldsymbol{A}$ versus the distance from the trailing end increase with increasing bubble volume, implying that the stresses grow faster (the stress singularity, if it exists, is stronger) for the larger bubbles. As noted in § 5.1, our results for the rise velocity of the bubble do not change when the spatial resolution is increased, indicating that the velocity and stress distributions away from

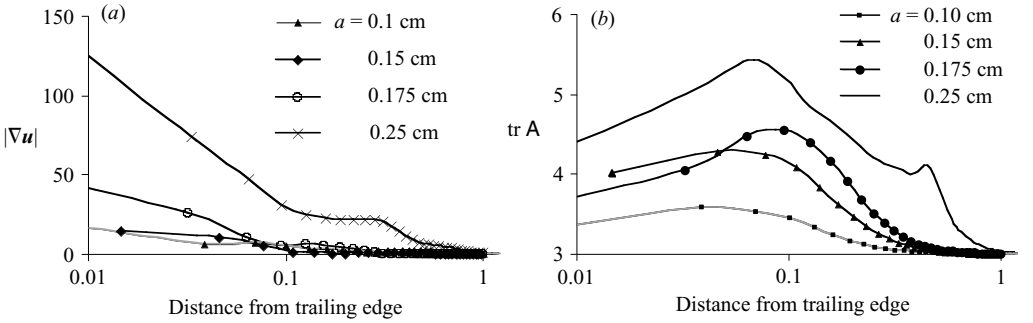

FIGURE 23. The magnitude of (*a*) the velocity gradient $|\nabla \boldsymbol{u}|$ and (*b*) tr$\boldsymbol{A}$ are shown as a function of the vertical distance from the trailing edge of the bubble; the parameters are $\eta_o = 10.25$ P, $\lambda_r = 0.1$ s, $c = 4.125$. The bubble radius is varied between 0.1 cm and 0.25 cm. The bubbles with radii 0.175 cm and 0.25 cm have a volume larger than the critical volume.

the trailing end are independent of the mesh resolution used (see Singh & Leal 1995). Specifically, Singh & Leal showed that for a viscoelastic flow around a $3\pi/2$ corner the stresses and velocity field away from the corner are not influenced by the mesh resolution used at the corner.

The existence of a two-dimensional cusp-shaped trailing end, or even a trailing end with a corner which is the case in our simulations, is an important issue because the stresses at the trailing end must balance the concentrated force due to the surface tension at the point of cusping or at a corner. (For the discretized problem, however, even when there is a corner, the surface tension force at the corner remains finite.) This requires that the stress at the cusping point has a non-integrable singularity and the dissipation rate of energy is infinite (see Joseph *et al.* 1991; Liu *et al.* 1995; Jeong & Moffatt 1992; Shikhmurzaev 1998, and references therein). From a physical point of view, this is not acceptable, and it was shown by Jeong & Moffatt that for a Newtonian fluid the interface remains smooth for finite capillary numbers, but the radius of curvature decreases exponentially with the capillary number. These authors also showed that the radius of curvature is of the order of molecular dimensions when it is computed based on the capillary number for experiments in which cusp-shaped interfaces were observed, indicating that the continuum theory may not be applicable and that some other physical mechanism must be introduced to model the problem (Shikhmurzaev 1998).

As already noted, in the discretized case even when the trailing end of the bubble develops a corner, the viscous and viscoelastic stresses, as well as the surface tension force at the cornered tail, remain finite, but grow as the finite element mesh is refined. The discretized problem, therefore, differs from the continuous problem in this sense.

In a Newtonian fluid, a true cusp cannot arise and the tip is always rounded with a small radius (the radius, however, may be of the order of molecular dimensions), but this may not necessarily be the case for viscoelastic fluids. Here, it is important to remember that since the viscoelastic stresses at the trailing end are extensional and cause the trailing end to pull out in the first place, they must be considered in the force balance at the cusped trailing end.

Furthermore, one must remember that the governing equations (5)–(7) for the Oldroyd-B model qualitatively capture the features of real viscoelastic liquids, including the fact that the stresses at the trailing end are extensional, but these equations may not necessarily capture the physics accurately once the radius of

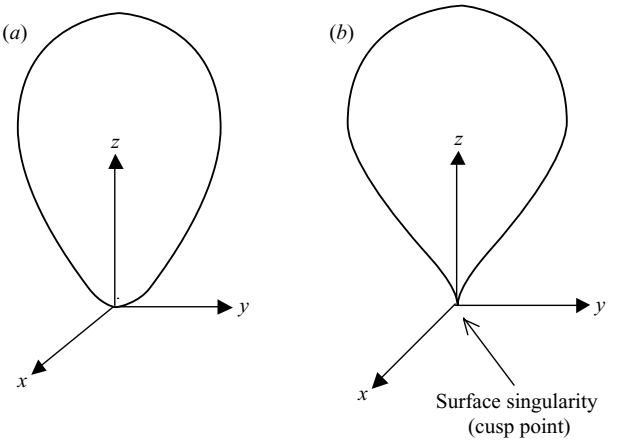

FIGURE 24. (*a*) Smooth bubble; (*b*) singular bubble.

curvature becomes of the order of molecular dimensions. In other words, the possibility that the bubbles rising in real viscoelastic liquids do develop cusp-shaped trailing ends should be considered.

If we assume that a bubble rising in a real viscoelastic liquid has a cusp-shaped trailing end, we must consider the fact that the integral of the surface tension force over its surface does not integrate to zero, unlike in the case of a smooth bubble. A cusped bubble, therefore, experiences an additional upward force that is concentrated at the point of cusping, which, of course, must be balanced by the viscous and viscoelastic stresses in the fluid. In this sense, the problem of a cusped bubble differs from that of a smooth bubble. This issue is considered in the next subsection.

5.4.2. *Analysis of surface tension forces on bubbles with singular surfaces*

Let B be a bubble with a smooth (C^2) closed surface S. The net surface force on the bubble, assuming a constant surface tension coefficient γ, is given by

$$\boldsymbol{F} = \int_S 2\,H\,\gamma\,\boldsymbol{n}\,\mathrm{d}A \tag{8}$$

where H is the mean curvature of S and $\boldsymbol{n}$ is the unit outer normal on S. It is known (see Blackmore & Ting 1985 and references therein) that $\boldsymbol{F}=0$. We shall show that for certain types of singularities in the surface at the trailing end of the bubble, $\boldsymbol{F}$ is no longer zero and there is a net upward force that accelerates the bubble to a larger terminal velocity. The smooth and the singular versions are illustrated in (figure 24*a*, *b*).

5.4.3. *Surface forces*

Recall that a vector-valued one-form in $\boldsymbol{R}^3$ is an expression of the form $\boldsymbol{A}\mathrm{d}x + \boldsymbol{B}\mathrm{d}y + \boldsymbol{C}\mathrm{d}z$, where $\boldsymbol{A}$, $\boldsymbol{B}$ and $\boldsymbol{C}$ are vectors representable in terms of the standard basis as $\boldsymbol{A}=\boldsymbol{A}_1\boldsymbol{i} + \boldsymbol{A}_2\boldsymbol{j} + \boldsymbol{A}_3\boldsymbol{k}$, etc. Similarly, a vector-valued two-form in $\boldsymbol{R}^3$ is an expression of the form $\boldsymbol{A}\mathrm{d}x \wedge \mathrm{d}y + \boldsymbol{B}\mathrm{d}x \wedge \mathrm{d}z + \boldsymbol{C}\mathrm{d}y \wedge \mathrm{d}z$, where terms such as $\mathrm{d}x \wedge \mathrm{d}y$ may be viewed as the often-used integration notation $\mathrm{d}x\mathrm{d}y$ including the orientation of the variables, according to the order x, y, z; so for example $\mathrm{d}x \wedge \mathrm{d}y = -\mathrm{d}y \wedge \mathrm{d}x$, since the orientation of x, y, z is opposite to that of y, x, z. Now, an example of a commonly used two-form is that associated with the differential of the surface area of

a smooth surface in $\boldsymbol{R}^3$ (such as employed in equations (9) and (13) below); namely

$$\mathrm{d}\boldsymbol{A} = \left| \frac{\partial \boldsymbol{x}}{\partial u} \times \frac{\partial \boldsymbol{x}}{\partial v} \right| \mathrm{d}u \wedge \mathrm{d}v,$$

where $\boldsymbol{x} = x\boldsymbol{i} + y\boldsymbol{j} + z\boldsymbol{k}$, u, v are parameters for the surface (so that $\boldsymbol{x} = \boldsymbol{x}(u, v)$ at least locally) and $\times$ denotes the standard cross-product. Consequently, the expression $\omega = H\boldsymbol{n}\mathrm{d}\boldsymbol{A}$ appearing in equations (8) and (9) is a vector-valued two-form.

The most direct way of showing that $\boldsymbol{F} = 0$ when S is C^2 is to observe that the right-hand side of equation (8) can be written as the surface integral of a vector-valued two-form

$$2\gamma \int_S H\,\boldsymbol{n}\,\mathrm{d}A = 2\gamma \int_S \omega \tag{9}$$

where

$$\omega = \omega_1\boldsymbol{i} + \omega_2\boldsymbol{j} + \omega_3\boldsymbol{k} = H\boldsymbol{n}\mathrm{d}\boldsymbol{A}, \tag{10}$$

and verify that the two-form ω is exact, namely, there exists a vector-valued one-form

$$\eta = \eta_1\boldsymbol{i} + \eta_2\boldsymbol{j} + \eta_3\boldsymbol{k} \tag{11}$$

on S such that

$$\mathrm{d}\eta = \mathrm{d}\eta_1\boldsymbol{i} + \mathrm{d}\eta_2\boldsymbol{j} + \mathrm{d}\eta_3\boldsymbol{k} = \omega. \tag{12}$$

Then, a simple application of Stokes' theorem yields the desired result (Blackmore & Ting 1985)

$$\boldsymbol{F} = 2\gamma \int_S \omega = 2\gamma \int_{\partial S} \eta = 2\gamma \int_{\emptyset} \eta = 0 \tag{13}$$

Since S has an empty boundary, ∂S is equal to $\emptyset$, where $\emptyset$ is the standard mathematical symbol used for the null set, not to be confused with the level-set function ϕ defined earlier in the manuscript.

The vector-valued one-form η is given as

$$\begin{aligned} 2\eta = -\boldsymbol{n} \times \mathrm{d}\boldsymbol{x} = (\langle \boldsymbol{n}, \boldsymbol{k}\rangle \mathrm{d}y - \langle \boldsymbol{n}, \boldsymbol{j}\rangle \mathrm{d}z)\boldsymbol{i} + (\langle \boldsymbol{n}, \boldsymbol{i}\rangle \mathrm{d}z - \langle \boldsymbol{n}, \boldsymbol{k}\rangle \mathrm{d}x)\boldsymbol{j} \\ + (\langle \boldsymbol{n}, \boldsymbol{j}\rangle \mathrm{d}x - \langle \boldsymbol{n}, \boldsymbol{i}\rangle \mathrm{d}y)\boldsymbol{k}, \end{aligned} \tag{14}$$

where $\boldsymbol{x} = (x, y, z) = x\boldsymbol{i} + y\boldsymbol{j} + z\boldsymbol{k}$, $\times$ denotes the usual vector cross-product in R^3, and $\langle \cdot, \cdot \rangle$ is the standard inner (dot) product of the vectors (Blackmore & Ting 1985).

It is natural to ask if equation (10) is still valid if the smoothness assumption on the surface S of the bubble is weakened. In particular, what happens if S has an isolated cusp-or cone-like point singularity or a line segment singularity? We show below that equation (10) holds for surfaces with isolated cusp-like or cone-like singularities, but an additional non-zero upward force due to surface tension occurs for a trailing-edge singularity composed of a line segment.

5.4.4. *Cusp and cone point singularities*

Here, we consider singularities at the trailing end of the bubble that can be modelled locally in the form (for $z \geqslant 0$):

$$z = \alpha r^q = \alpha(x^2 + y^2)^{q/2} (\alpha > 0, q \text{ is a positive rational}, 0 < q \leqslant 1) \tag{15}$$

in a neighbourhood of the region (trailing point) in R^3, as illustrated in figure 25(a, b).

In the case under consideration, the bubble surface is smooth except at the origin, so we can apply Stokes' theorem to the portion S_{z_o} of the surface S on or above the

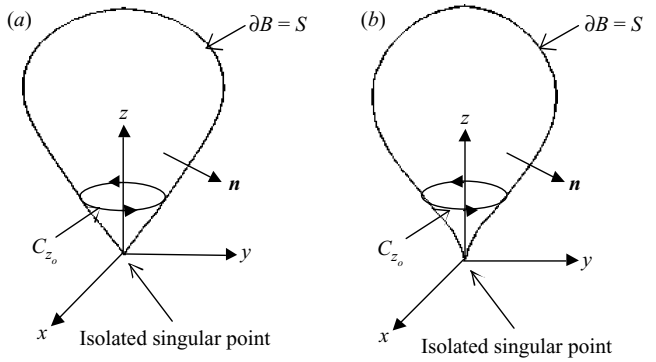

FIGURE 25. (*a*) Cone point at origin ($q = 1$). (*b*) Cusp point at origin ($0 < q \leqslant 1$).

plane $z = z_o (z_o > 0)$. If z_o is sufficiently small, it follows from equation (15) that the plane $z = z_o$ intersects S in the planar curve

$$C_{z_o} : x = \left(\frac{z_o}{\alpha}\right)^{1/q} \cos\theta,\ y = \left(\frac{z_o}{\alpha}\right)^{1/q} \sin\theta,\ z = z_o \qquad (0 \leqslant \theta \leqslant 2\pi). \tag{16}$$

Note that we have chosen the orientation of C_{z_o} to be consistent with the orientation of S_{z_o}. From equation (15) we compute that the unit outward normal to S in a small neighbourhood of C_{z_o} is

$$\boldsymbol{n} = \left[x^2 + y^2 + \frac{1}{q^2\alpha^{4/q}} z^{2(2-q)/q}\right]^{-1/2} \left(x\,\boldsymbol{i} + y\,\boldsymbol{j} - \frac{1}{q\alpha^{2/q}} z^{(2-q)/q}\boldsymbol{k}\right). \tag{17}$$

Now, from Stokes theorem and equations (14), (16) and (17), we compute that

$$\begin{aligned}
\int_{S_{z_o}} H\,\boldsymbol{n}\,\mathrm{d}A &= \int_{S_{z_o}} \omega = \int_{C_{z_o}} \eta = -\frac{1}{2}\int_{C_{z_o}} \boldsymbol{n} \times \mathrm{d}\boldsymbol{x} \\
&= \left(\frac{z_o}{\alpha}\right)^{1/q} \left[1 + \frac{1}{q^2\alpha^{2/q}} z_o^{2(1-q)/q}\right]^{-1/2} \\
&\quad \times \int_0^{2\pi} \left\{-\frac{2}{q\alpha^{3/q}} z_o^{(3-q)/q} \cos\theta\,\boldsymbol{i} - \frac{2}{q\alpha^{3/q}} z_o^{3-q/q} \sin\theta\,\boldsymbol{j} - \left(\frac{z_o}{\alpha}\right)^{2/q} \boldsymbol{k}\right\} \mathrm{d}\theta \\
&= -\pi \left(\frac{z_o}{\alpha}\right)^{-1/q} \left[1 + \frac{1}{q^2\alpha^{2/q}} z_o^{2(1-q)/q}\right]^{-1/2} \to 0 \quad \text{as } z_o \to 0^+.
\end{aligned} \tag{18}$$

Accordingly, equation (13) also holds for a bubble having either a cone or a cusp point singularity on its trailing edge.

5.4.5. *Chisel type singularity*

In this section we consider a bubble whose surface S has a whole line segment of singular points (chisel edge) on its trailing edge as shown in figure 26.

For sufficiently small $z(> 0)$, such a chisel-edge can be represented as follows:

$$\left(\frac{x}{a + \beta z^{1/q}}\right)^2 + \left(\frac{y}{\beta z^{1/q}}\right)^2 = 1, \tag{19}$$

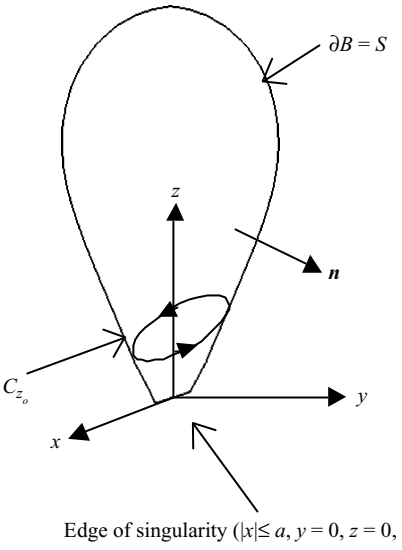

FIGURE 26. Chisel edge along the x-axis.

where $\beta > 0$ and $0 < q \leqslant 1$, as in equation 15. If $z_o > 0$ is sufficiently small, it follows from Equation 19 that the plane $z = z_o$ intersects in the ellipse

$$C_{z_o} : x = \left(a + \beta\, z_o^{1/q}\right) \cos\theta,\ y = \beta\, z_o^{1/q}\ \sin\theta, z = z_o \qquad (0 \leqslant \theta \leqslant 2\pi) \tag{20}$$

which has an orientation consistent with that of $S_{z_a} := S \cap \{(x, y, z) : z \geqslant z_0\}$.

Observe that when $z_o \to 0^+$, the ellipse degenerates into a line segment $|x| \leqslant a$ on the x-axis coinciding with the singular chisel edge on the bubble surface. From equation (19) we calculate the outward unit normal to S in a small neighbourhood of the curve C_{z_o} to be

$$\begin{aligned} \boldsymbol{n} = &\left\{ \frac{x^2}{(a+\beta z^{1/q})^4} + \frac{y^2}{(\beta z^{1/q})^4} + \frac{\beta^2}{q^2} z^{2(1-q)/q} \left[\frac{x^2}{(a+\beta z^{1/q})^3} + \frac{y^2}{(\beta z^{1/q})^3} \right]^2 \right\}^{-1/2} \\ &\times \left\{ \left(\frac{x}{(a+\beta z^{1/q})^2} \right) \boldsymbol{i} + \left(\frac{y}{(\beta z^{1/q})^2} \right) \boldsymbol{j} + \left(\frac{\beta}{q} z^{(1-q)/q} \left[\frac{x^2}{(a+\beta z^{1/q})^3} + \frac{y^2}{(\beta z^{1/q})^3} \right] \right) \boldsymbol{k} \right\}. \end{aligned} \tag{21}$$

Now, using equations (19)–(21) and Stokes theorem, we readily compute that for small $z_o > 0$, we have

$$\begin{aligned} \Phi(z_o) :&= \int_{S_{z_o}} H\, \boldsymbol{n}\, \mathrm{d}A = \int_{S_{z_o}} \omega = \int_{C_{z_o}} \eta = -\frac{1}{2} \int_{C_{z_o}} \boldsymbol{n} \times \mathrm{d}\boldsymbol{x} \\ &= \frac{1}{2} \left\{ \frac{\cos^2\theta}{(a+\beta z_o^{1/q})^2} + \frac{\sin^2\theta}{(\beta z_o^{1/q})} + \frac{\beta^2}{q^2} z_o^{2(1-q)/q} \left[\frac{\cos^2\theta}{(a+\beta z_o^{1/q})} + \frac{\sin^2\theta}{(\beta z_o^{1/q})} \right]^2 \right\}^{-1/2} \\ &\quad \times \int_0^2 \left\{ -\frac{\beta}{q} z_o^{1-q/q} \left[\left(\frac{\beta z_o^{1/q}}{a+\beta z_o^{1/q}} \cos^3\theta + \sin^2\theta\, \cos\theta \right) \boldsymbol{i} \right. \right. \\ &\quad + \left(\cos^2\theta\, \sin\theta + \frac{a+\beta z_o^{1/q}}{\beta z_o^{1/q}} \sin^2\theta \right) \boldsymbol{j} \Big] - \left[\left(\frac{a+\beta z_o^{1/q}}{\beta z_o^{1/q}} \right) \sin^2\theta \right. \\ &\quad \left. \left. + \left(\frac{\beta z_o^{1/q}}{a+\beta z_o^{1/q}} \right) \cos^2\theta \right] \boldsymbol{k} \right\} \mathrm{d}\theta. \end{aligned} \tag{22}$$

We now calculate $\lim_{z_0 \to 0^+} \Phi(z_o)$ for the two cases: (i) $0 < q < 1$ and (ii) $q = 1$. In case (i), it is straightforward to show that

$$\lim_{z_0 \to 0^+} \Phi(z_o) = -2a\boldsymbol{k} \qquad (0 < \mathrm{q} < 1). \tag{23}$$

For $q = 1$, calculating the limit is slightly more complicated, but still routine. We now sketch the computation. If we intersect the bubble near $z = 0$ with the plane $x = 0$, we find from equation (19) that

$$\left(\frac{y}{\beta z}\right)^2 = 1 \Rightarrow y = \pm \beta z,$$

and therefore conclude that the chisel edge is the edge of a symmetric wedge with sides defined by $y \pm \beta z = 0$ in R^3. Observe that the normals for the sides of the wedge are $(1 + \beta^2)^{-1/2}(\boldsymbol{j} - \beta \boldsymbol{k})$ for $y - \beta z = 0$ and $(1 + \beta^2)^{-1/2}(-\boldsymbol{j} - \beta \boldsymbol{k})$ for $y + \beta z = 0$ and that when $0 < q < 1$, the limiting normal directions are $\boldsymbol{j}$ and $-\boldsymbol{j}$, respectively. Consequently, in case (ii), we obtain

$$\lim_{z_0 \to 0^+} \Phi(z_o) = -\frac{2a}{\sqrt{1 + \beta^2}} \boldsymbol{k} \quad (q = 1). \tag{24}$$

In either of the above two cases, we see that there is an unbalanced force on the singular bubble due to surface tension, which must be balanced, according to Newton's third law, by an additional upward force on the bubble given by

$$\boldsymbol{F}_+ = \begin{cases} 4\gamma a \boldsymbol{k} & (0 < q < 1). \\ \dfrac{4\gamma a}{\sqrt{1+\beta^2}} \boldsymbol{k} & (q = 1). \end{cases} \tag{25}$$

Therefore, the development of a chisel-edge singularity on the trailing end of the bubble should be accompanied by an increase in the upward force (due to interfacial tension) that acts on the bubble that is proportional to the width of the singular edge.

6. Discussion and concluding remarks

The transient and steady-state motions of bubbles rising in viscoelastic liquids subjected to buoyancy were analysed using a three-dimensional finite-element-based numerical scheme. The viscoelastic fluid was modelled using the Oldroyd-B constitutive model and the level-set method was used to track the interface. The results of the direct numerical simulations were then used to analyse the transient behaviour of rising bubbles, the sharp increase in the terminal velocity in the velocity–volume plot at a critical bubble volume, and the velocity and stress distributions in the wake of the bubbles. These analyses were carried out for different values of the polymer concentration parameter c, the relaxation time λ_r, and the bubble radius a, while keeping other parameters such as the interfacial tension, density ratio, viscosity ratio and the zero-shear viscosity constant.

Our simulation results indicate that a bubble released from rest first accelerates and, once the viscoelastic stresses become significant, either decelerates until reaching a constant terminal velocity or exhibits an oscillating velocity. After the viscoelastic stresses become substantial, the bubble either assumes a steady shape or continues to deform, depending on the choice of parameters. When the viscoelastic stresses at the

interface are sufficiently large, the trailing end of the bubble is pulled out due to the extensional nature of the viscoelastic stresses in this region, and when this happens we find that the rise velocity of the bubble begins to increase again and reaches a much larger steady value.

Furthermore, our simulations have shown that when the bubble volume is increased, while keeping all other parameters constant, the bubble begins to deform from an approximately spherical shape first to a prolate shape and then, at a critical volume, to a shape with a cusp-like trailing end. When the terminal velocity is plotted as a function of the bubble volume, a steep increase in the terminal velocity is observed at the value of the bubble volume which coincides with the critical volume at which the bubble develops an elongated cusp-like trailing end. The jump in the rise velocity at the critical volume increases as the polymer concentration parameter c increases. The capillary and Deborah numbers at which the bubble shape develops a cusped trailing end are $O(1)$.

Another interesting feature is that the flow pattern in the wake of a bubble rising in a viscoelastic liquid is quite different from that in a Newtonian liquid. Specifically, in the former case, for certain parameter values there is an additional vortex ring in the surrounding flow, corresponding to the existence of a negative wake. Our numerical and analytical results indicate that the asymmetric, cusped, bubble shape, the presence of an additional vortex ring compared to the Newtonian case and the change in the velocity field in response to the change in the bubble shape, all contribute to the jump in the bubble velocity at a critical bubble volume for the appropriate parameter range. Note that since the potential presence of surfactants is not considered here, the jump in the rise velocity is not due to a surfactant effect in our calculations.

A sharp corner in the discretized problem, possibly corresponding to a cusp in the physical problem, develops at the trailing end of the bubble because of the extensional viscoelastic stresses. The bubble then reaches a steady state in which its shape is maintained by a balance of the forces due to the surface tension and the viscoelastic stresses at the trailing end. In simulations, after the bubble develops a trailing end with a sharp corner, the integral of the surface tension force over the bubble surface is no longer zero, resulting in an upward force which, however, remains small compared to the buoyant weight (less than approximately 1% to 2% of the buoyant weight). As noted in this paper, this would also be true if the bubble developed a two-dimensional cusp-shaped trailing end. When the line segment representing the cusp-shaped, or a sharp-cornered, trailing edge is in the (x, y)-plane (see figure 2), there is a net surface tension force in the upward direction, i.e. the integral of the surface tension force over the bubble surface is non-zero. The extensional viscoelastic stresses near the trailing end cause the formation of the cusped, or cornered in the discretized case, trailing edge.

It is, however, important to note that the additional surface tension force which can arise due to the formation of a cusp- or corner-shaped trailing end is too small to explain the large increase in the rise velocity. In order to show this, we consider a bubble of radius 0.2 cm with a cusp-shaped trailing edge of width 0.05 cm, i.e. one fourth of the bubble radius. The net surface tension force on this bubble in the upward direction is $0.1\sigma g \approx 1.0$ dyn, assuming that the surface tension is 10 dyn cm^{-1} which is the value used in our simulations. If one neglects the bubble density compared with the density of the ambient fluid, and assume that the latter is one, the buoyant weight of the bubble takes the value $(4\pi a^3/3)\rho_L g \approx 32.9$ dyn. It results that, for a bubble of this size, the additional surface tension force is only about 3% of the buoyant weight, and thus not large enough to explain the observed large increase in the rise

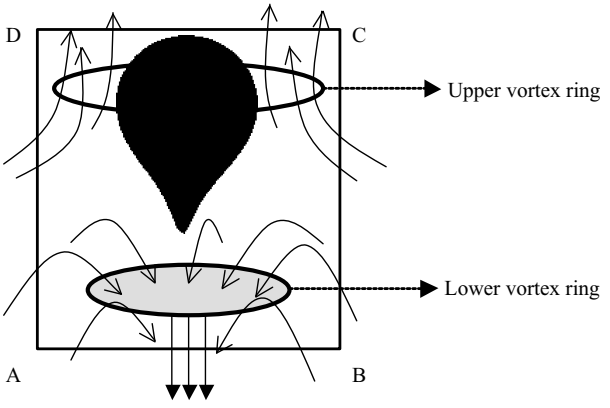

FIGURE 27. Sketch of a box-shaped control volume (front view marked ABCD) which encloses the bubble. Because of the presence of the lower vortex ring, the fluid velocity at the bottom of the control volume is in the downward direction, thus resulting in a negative wake.

velocity. If, on the other hand, the surface tension is $70\,\mathrm{dyn\,cm^{-1}}$, as is the case for the air–water interface, it would be about 20% of the buoyant weight.

Furthermore, the jump in the rise velocity at higher values of c is much larger, even though the additional surface tension force due to the formation of the cusp-like trailing end remains approximately the same. This suggests that the global modification in the velocity field in the ambient fluid, which is more substantial at higher values of c, is probably the reason for the several-fold increase in the rise velocity of the bubble.

We also point out that after the bubble develops a cusp-like trailing end, the shape does not change significantly with the polymer concentration parameter c, whereas the magnitude of the jump does vary significantly. The magnitude of the negative velocity in the wake also increases with increasing c. This, again, indicates that the flow modification, which is more substantial at higher values of c, is important in determining the magnitude of the jump.

It is instructive to apply momentum conservation to a box-shaped control volume enclosing the bubble and travelling with the bubble. In figure 27 the front view of this control volume is marked by ABCD. In steady state, the sum of the net momentum flux through the sidewalls, the forces acting on the control volume's surface and the body force must be equal to zero. In the case of a Newtonian fluid, the fluid velocity at the bottom and top surfaces of this control volume is directed upwards and the net momentum flux through these surfaces is determined by the difference in the velocity magnitudes. In the case of a viscoelastic fluid, at the top of the control volume the velocity is directed upwards, while the fluid velocity at the bottom, when a negative wake is present, is directed downwards. Therefore, in the viscoelastic case, the net momentum flux contribution to the control volume from the top and bottom surfaces is guaranteed to be positive, which implies that the momentum flux from these two surfaces results in a thrust in the upward direction. This, in a way, is similar to the case of a jet engine where the thrust in the forward direction is generated by ejecting gases at a fast speed in the direction opposite to the motion of the aircraft (Newton's third law); the difference is that in the present study the negative wake arises simply due to the viscoelasticity of the fluid and does not require additional actuation. In the present study, the upward thrust due to the momentum flux (because of the presence

of the negative wake) is, of course, countered by the shear and normal forces acting on the surface of the control volume.

The support of the National Foundation under grants 0626123 (P.S.) and 0626070 (N.A.) is greatly appreciated.

REFERENCES

Arigo, M. T. & McKinley, G. H. 1998 An experimental investigation of negative wakes behind spheres settling in a shear-thinning viscoelastic fluid. *Rheol. Acta* **37**(4), 307–327.

Astarita, G. & Apuzzo, G. 1965 Motion of gas bubbles in non-Newtonian liquids, *AIChE J.* **11**(5), 815–820.

Barnett, S. M., Humphrey, A. E. & Litt, M. 1966 Bubble motion and mass transfer in non-Newtonian fluid *AIChE J.* **12**(2), 253–259.

Belmonte, A. 2000 Self oscillations of a cusped bubble rising through a micellar solution. *Rheol. Acta* **39**, 554–559.

Bisgaard, C. 1983 Velocity fields around spheres and bubbles investigated by laser-Doppler anemometry. *J. Non-Newtonian Fluid Mech.* **12**, 283–302.

Blackmore, D. & Ting, L. 1985 Surface integral of its mean curvature vector. *SIAM Rev.* **27**-4.

Bristeau, M. O., Glowinski, R. & Periaux, J. 1987 Numerical methods for Navier-Stokes equations. Application to the simulation of compressible and incompressible flows. *Comput. Phys. Rep.* **6**, 73.

Calderbank, P. H., Johnson, D. S. & Loudon, J. 1970 Velocity fields around spheres and bubbles investigated by laser-doppler anemometry. *Chem. Engng. Sci.* **25**, 235–256.

Chen, S. & Rothstein, J. P. 2004 Flow of a wormlike micelle solution past a falling sphere. *J. Non-Newtonian Fluid Mech.* **116**, 205–234.

Chilcott, M. D. & Rallison, J. M. 1988 Creeping flow of dilute polymer solutions past cylinders and spheres. *J. Non-Newtonian Fluid Mech.* **29**, 381.

Funfschilling, D. & Li, H. Z. 2001 Flow of Non-Newtonian fluids around bubbles: PIV measurements and birefringence visualization, *Chem. Engng Sci.* **56**, 1137–1141.

Glowinski, R., Tallec, P., Ravachol, M. & Tsikkinis, V. 1992 In *Finite Elements in Fluids*, (ed. T. J. Chung), vol. 8, chap. 7. Hemisphere.

Glowinski, R. & Pironneau, O. 1992 Finite element methods for Navier-Stokes equations. *Annu. Rev. Fluid Mech.* **24**, 167.

Glowinski, R., Pan, T. W., Hesla, T. I. & Joseph, D. D. 1999 A distributed Lagrange multiplier/fictitious domain method for particulate flows. *Intl J. Multiphase Flows* **25**(5), 755.

Handzy, N. Z. & Belmonte, A. 2004 Oscillatory motion of rising bubbles in wormlike micellar fluid with different microstructures. *Phys. Rev. Lett.* **92**, 124501.

Happel, J. & Brenner, H. 1981 *Low Reynolds Number Hydrodynamics: with special applications to particulate media.* Springer.

Hassagar, O. 1979 Negative wake behind bubbles in non-Newtonian liquids. *Nature* **279**, 402–403.

Herrera-Velarde, J. R. Zenit, R., Chehata, D. & Mena, B. 2003 The flow of non-Newtonian fluids around bubbles and its connection to the jump discontinuity. *J. non-Newtonian Fluid Mech.* **111**, 199–209.

Jayaraman, A. & Belmonte, A. 2003 Oscillations of a solid sphere falling through a wormlike micellar fluid. *Phys. Rev.* E **67**, 65301.

Jeong, J. & Moffatt, H. K. 1992 Free-surface cusps associated with flow at low Reynolds number. *J. Fluid Mech.* **241**, 1–22.

Joseph, D. D., Nelson, J., Renardy, M. & Renardy, Y. 1991 Two-dimensional cusped interfaces. *J. Fluid Mech.* **223**, 383–409.

King, M. J. & Walters, N.D. 1972 The unsteady motion of a sphere in an elastico-viscous liquid. *J. Phys.* D: *Appl. Phys.* **5**, 141–150.

Leal, L. G., Skoog, J. & Acrivos, A. 1971 On the motion of gas bubbles in a viscoelastic fluid. *Can. J. Chem. Engng* **49**, 569–575.

Liu, Y. J., Liao, T. Y. & Joseph, D. D. 1995 A two-dimensional cusp at the trailing edge of an air bubble rising in a viscoelastic liquid. *J. Fluid Mech.* **304**, 321–342.

Marchuk, G. I. 1990 Splitting and alternate direction methods. In *Handbook of Numerical Analysis* (ed. P. G. Ciarlet & J. L. Lions), Vol. 1, P. 197. North-Holland.

McKinley, G. H. 2001 *Transport Processes in Bubbles, Drops and Particles.* (ed. R. P. Chhabra & D. DeKee), 2nd edn, Taylor Francis.

Noh, D. S., Kang I. S. & Leal, L. G. 1993 Numerical solutions for the deformation of a bubble rising in dilute polymeric fluids. *Phys. Fluids* **5**, 1315–1332.

Philippoff, W. 1937 Viscosity characteristics of rubber solution. *Rubber Chem. Tech.* **10**, 76.

Pillapakkam, S. B. & Singh, P. 2001 A level-set method for computing solutions to viscoelastic two-phase flow. *J. Comput. Phys.* **174**, 552–578.

Ramaswamy, S. & Leal, L. G. 1999 The deformation of a viscoelastic drop subjected to steady uniaxial extensional flow of a Newtonian fluid. *J. Non-Newtonian Fluid Mech.* **85**, 127.

Rodrigue, D., Chhabra, R. P. & Chan Man Fong, C. F. 1996 An experimental study of the effect of surfactants on the free rise velocity of gas bubbles. *J. Non-Newtonian Fluid Mech.* **66**, 213–232.

Rodrigue, D., Chhabra, R. P. & Fong, C. F. C. M. 1998 Bubble velocities: further developments on the jump and discontinuity. *J. Non-Newtonian Fluid Mech.* **79**, 45–55.

Shikhmurzeav, Y. D. 1998 On cusped interfaces. *J. Fluid Mech.* **359**, 131–328.

Singh, P. & Joseph, D. D. 2000 Sedimentation of a sphere near a vertical wall in an Oldroyd-B fluid. *J. Non-Newtonian Fluid Mech.* **94**, 179–203.

Singh, P., Joseph, D. D., Hesla, T. I., Glowinski, R. & Pan, T.W. 2000 A distributed Lagrange multiplier/fictitious domain method for viscoelastic particulate flows. *J. Non-Newtonian Fluid Mech.* **91**, 165.

Singh, P. & Leal, L.G. 1993 Finite element simulation of the start-up problem for a viscoelastic problem in an eccentric cylinder geometry using third-order upwind scheme *Theor. Comput. Fluid Dyn.* **5**, 107–137.

Singh, P. & Leal, L. G. 1994 Computational studies of dumbbell model fluids in a co-rotating two-roll mill. *J. Rheol.* **38**, 485–517.

Singh, P. & Leal, L. G. 1995 Viscoelastic flows with corner singularities. *J. Non-Newtonian Fluid Mech.* **58**, 279–313.

Sussman, M., Smereka, P. & Osher, S. 1994 A level set approach for computing solutions to incompressible two-phase flow. *J. Comput. Phys.* **114**, 146.

Wagner, A. J., Giraud, L. & Scott, C. E. 2000 Simulations of a cusped bubble rising in a viscoelastic fluid with a new numerical method. *Comput. Phys. Comm.* **129**, 227–231.

Zheng, R. & Pan-Thien, N. 1992 A boundary element simulation of the unsteady motion of a sphere in a cylindrical tube containing a viscoelastic fluid. *Rheol. Acta* **31**, 323–332.